2021

Contact Fatigue of Spur Gear Operating Under Starved Lubrication Condition

Aparna Udthala
Wright State University

CONTACT FATIGUE OF SPUR GEAR OPERATING UNDER STARVED LUBRICATION CONDITION

A Thesis submitted in partial fulfillment of the
requirements for the degree of
Master of Science in Mechanical Engineering

by

APARNA UDTHALA

B.E, Osmania University, India, 2018

2021

Wright State University

WRIGHT STATE UNIVERSITY

GRADUATE SCHOOL

11/23/2020

I HEREBY RECOMMEND THAT THE THESIS PREPARED UNDER MY SUPERVISION BY Aparna Udthala ENTITLED Contact Fatigue of Spur Gear Operating Under Starved Lubrication Condition BE ACCEPTED IN PARTIAL FULFILLMENT OF THE REQUIREMENTS FOR THE DEGREE OF Master of Science in Mechanical Engineering.

_____
Sheng Li, Ph.D.
Thesis Director

_____
Raghavan Srinivasan, Ph.D., P.E.
Chair, Mechanical and Materials
Engineering Department

Committee on Final Examination:

_____
Sheng Li, Ph.D.

_____
Ahsan Mian, Ph.D.

_____
Joy Gockel, Ph.D.

_____
Barry Milligan, Ph.D.
Interim Dean of the Graduate School

ABSTRACT

Udthala, Aparna. M.S.M.E, Department of Mechanical and Material Engineering, Wright State University, 2021. Contact Fatigue of Spur Gear Operating Under Starved Lubrication Condition

This study describes contact fatigue behavior of spur gear contacts operating under mixed elastohydrodynamic condition. The focus is placed on the starvation effect on fatigue crack initiation. With the model, parametric simulations are carried out with different contact parameters. In the process, the lubricant supply is varied to alter the lubrication condition from fully flooded to severely starved circumstance. Multi-axial stress fields induced by surface normal and tangential tractions are evaluated, whose amplitudes and means are used in a multi-axial fatigue criterion to determine the crack initiation life. It is found a lower lubricant viscosity elongates fatigue life when severe starvation occurs, which is opposite to the EHL rule under fully flooded lubrication condition. However, it's in line with the experimental observation [1], where film thickness was shown to increase when moving from high viscosity base oil to a lower one under starvation condition.

TABLE OF CONTENTS

LIST OF FIGURES

LIST OF TABLES

Tables **Page**

ACKNOWLEGMENT

Firstly, My sincere gratitude to my advisor and Professor **Dr. Sheng Li** for his consistent support and guidance throughout my research project. This was a great opportunity to work and learn under Dr. Sheng Li, who also had introduced me to research work side for first time. Continuously provided encouragement and always willing and enthusiastic to assist in any way. Which helped me in gaining knowledge in Tribology and sharpen my skills.

I extent sincere gratitude to my committee members, **Dr. Ahsan Mian** and **Dr. Joy Elizabeth Gockel** for their intellectual discussions, feedback and intriguing comments throughout the research.

I will be always thankful to Wright State University for all immense opportunities and resources for my master's journey.

A special Thanks to my parents **Mr. Srinivas Udthala** and **Mrs. Bhagya Laxmi Udthala** for their extreme support and constant encouragement in my research work and to my younger brothers for their motivation and support in my difficult times.

CHAPTER -1

INTRODUCTION

1.1. BACKGROUND STUDY AND MOTIVATION

Mechanical parts, like rolling element are mostly used in Industries today. The main purpose of this elements is to transmit high loads, motion etc. During this process they come in to contact to optimize the performance and to transmit power smoothly. Lubrication film between contacting bodies is essential, which minimizes friction, wear, and prolonging life. This film separates the contact surfaces, accommodates the speed differences, and avoid contact heating. Lubricant thickness depends up on contact surfaces regime operating under. Previous studies has classified fundamental lubricant regime for contact surfaces.

- Full film/Hydrodynamic – Contact surface are completely separated by full unbroken film of lubricant.
- Elastohydrodynamic – For surfaces under high loads, this regime is governed by a sudden reduction of lubricant film thickness which causes an increase in lubricant viscosity. When lubricant film becomes rigid, it causes temporary elastic deformation of contact surface.
- Mixed – Where there is a mixture of asperity interaction and lubrication separation between contact surface

- Boundary – Contact surfaces are close enough that substantial metal to metal contact of opposing asperities occurs.

In severity operation conditions (high-speeds, grease lubrication, limited lubrication supply) in lubricated contact has led to the decrease of film thickness and tends to failure mode, this failure mode is stated under starvation conditions. The most common failure in tribosystem are fatigue, wear and scuffing, these are mainly related to fatigue, lubrication and wear conditions. Starvation may occur mainly due to insufficient supply of lubrication, inlet lubrication film break-down and surface failure. Some of the factors influencing starvation occurrence are

- Velocities
- Applied load
- Material properties
- Contact tribology.

Owing to the improvement of manufacturing techniques in the past decades, the occurrence of impurities in modern steel alloys becomes much less frequent. Starvation effects in electrohydrodynamic lubricant (EHL) contact can lead to film break down and increase in contact pressure, with this high contact pressure micro pitting takes place.

(a)

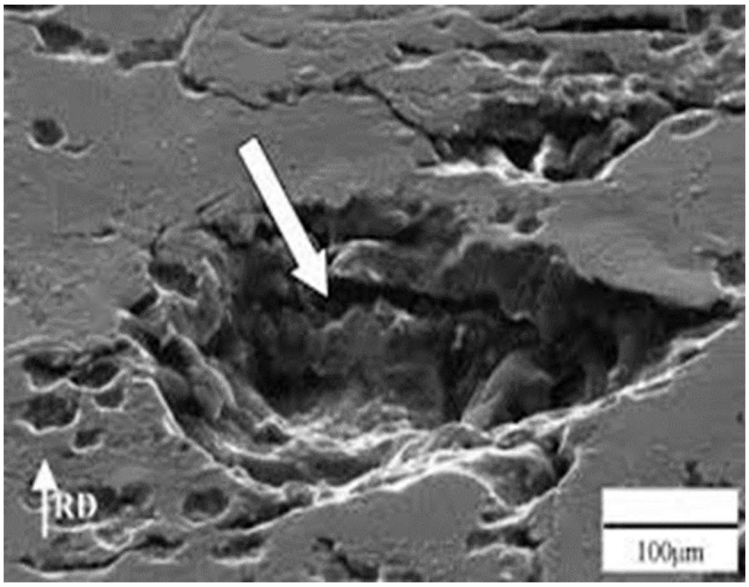

(b)

Figure 1.1: (a) Pitting in gears, and (b) Microscopic image of a pit

Source: www.google.com/pitting in gear

Macro-pitting is a major failure mode of gear contacts, where surface roughness is usually significant and tooth force is commonly large. Webster and Norbart [44] founded Micro-pits tended to appear on the surface with negative sliding. It was also shown that the reduction of micro pitting could be achieved through the reduction of slid to roll ratio and/or roughness amplitude. In a group of early studies [2-4], macro-pitting failures were reported to initiate below contact surfaces, and thus referred as sub-surface nucleated failure. The associated pitting failure were frequently observed to arise from surface-initiated fatigue cracks [5-8], where near surface stresses that are highly influenced by contact tribological behavior dictate the fatigue crack nucleation. As surface breaking fatigue cracks turn into the main cause of rolling contact fatigue (RCF) failure for modern cleaner materials. This study, therefore, focuses on the computational investigation of RCF surface crack initiation propagation is out of the current scope. The influential parameters on surface fatigue crack nucleation are diverse, including surface roughness, lubricant properties, and operating conditions. Starvation film thickness has been measured for series of greased and the results have been compared to the fully flooded values. In this work, the generalized Newtonian Reynolds equation with a cavitation algorithm [30] incorporated, proposed by Li and Masse [29], is implemented in conjunction with an asperity contact equation and a film thickness equation to describe the surface tribological behavior. Most recently, Li and Masse [29] proposed a thermal mixed EHL model for starved line contacts, incorporating measured viscosity dependences on pressure, temperature, and shear rate. These realistic lubricant property descriptions allow the proper and accurate prediction of fatigue life of the rolling elements. Using the model developed, a parametric simulation is

performed to show fatigue life variations with starvation severity, surface roughness amplitude, lubricant viscosity (by varying lubricant temperature), and normal load

1.2. LITERATURE REVIEW

Early studies on lubrication in counter formal contacts focused mainly on cases under fully flooded conditions and notable achievement have been made in this aspect. First calculations of lubricant film thickness conducted by Dawson and Higginson and Hamrock and Dowson, stating film thickness as a function of speed, load, geometry, material, lubrication properties. Their predictions were validated for smooth steady state and fully flooded contacts. In view of the above investigations, and data obtained from fully flooded lubrication condition experimentation were adopted to study the fatigue life in starvation lubrication conditions. When lubrication starvation is of concern, such as rolling mechanical elements operating with limited lubricant supply [1, 18], loss of lubricant [19], or inlet blockage by wear and fatigue debris [20], most works focused on the starvation impact on friction, wear and scuffing failure. Thus it is important to estimate the film thickness reduction, in order to adjust the predicated life, the surface finish on other hand, it would also be advantageous to know the minimum quantity of oil required to adequately lubricate a contact under given operating conditions.

For instance, Ali et al. [21] studied the friction behavior of a point contact, showing micro-scale surface texturing can increase the friction performance under starved lubrication condition. In starvation of electrohydrodynamic lubrication contact can lead to increase of pressure condition as well as excessive friction and wear caused by direct surface interactions.

Lewis et al. [22] assessed the performance of different greases in friction and wear under fully lubricated and starved lubrication conditions, observing higher wear rates when the lubrication is starved.

To model the tribological behavior between two surfaces that roll against each other with insufficient lubricant supply (starvation), a group of early works [25, 26] assumed perfectly smooth surfaces and excluded temperature variations across EHL conjunctions. Considering an Eyring non-Newtonian fluid, Yang et al. [27] included flash temperature prediction for smooth surface contacts operating under starved lubrication condition. Assuming exponential viscosity dependence on pressure, and Newtonian relationship between viscous shear and shear rate, Pu et al. [28] modeled flash temperature rises of rough surface contacts when lubrication is starved. Employing a twin-disk contact pair lubricated through a lubrication jet, Querlioz et al. [23] experimentally measured the fatigue lives under starved lubrication condition for two different lubricants, showing substantial fatigue life reduction as starvation severity increases. In the tests, the surfaces of the specimens were pre-dented to accelerate macro-pitting failure. Adopting sinusoidal surface roughness profiles, Labiau et al. [24] showed that starvation reduced fatigue life significantly. Extensive experimental studies have been conducted in literature to investigate the influences of various potential factors on micro-pitting, Takuda et.al[4] showed that surface roughness was a key parameter influencing micro-pitting even under full-film lubrication. On the aspect of rolling contact fatigue in the form of macro-pitting, however, the relevant investigations are relatively sparse and are mostly experimental In these works, crack nucleation locations were found to be tightly related to inclusions, voids, or defects present in material beneath the surface. The test results indicated that a run-in stage with higher contact pressures and lower velocity reduce number of micro pits.

The surface roughness due to gear finishing processes, such as grinding and shaving, can substantially elevate contact pressures by introducing local asperity contacts where lubrication film breaks down [9, 10]. Considering the coexistence of asperity contacts and hydrodynamic lubrication, extensive modeling works have been carried out to describe the lubricated rolling contact fatigue behavior. Snidle and Evans [13] simulated a spur gear contact using a line contact of two cylinders. Zhu et al. [14] proposed a 3D line contact model to include surface roughness variation along gear tooth width direction, although such variation is usually limited. Point contact models [5, 15] have also been presented, such that gear tooth flanks that are significantly crowned can be analyzed in a proper way. Considering the transient effects associated with time-varying tooth force, contact radii, and surface velocities as gears rotate in mesh, Li et al. [6] adopted a transient mixed electrohydrodynamic lubrication (EHL) model [10] that was specifically designed for gear contacts to evaluate surface contact stresses. Further, Li and Anisetti [16] included the interactions between gear dynamics and gear tribological behavior into surface contact fatigue modeling, showing evident tribo-dynamic impacts on surface breaking crack nucleation. All these studies pointed to the critical role of surface roughness in surface initiated rolling contact fatigue. On the experimental side, twin-disk type of set-up [5, 17] or standard FZG that directly uses gear specimens [6] have been utilized to investigate the effects of surface roughness, lubricant temperature, lubricant additives, and load on macro-pitting failure, confirming the findings of the computational studies. Considering engineering surface profiles as well as electrohydrodynamic lubrication (EHL) behavior, a number of researchers [5,14,15] showed significant near surface stress concentration induced by surface asperity interactions under mixed lubrication conditions.

Mixed EHL model used to determine the instantaneous surface contact pressure and traction distribution. The normal contact pressure and tangential shear distributions yielded from the tribological formulation are used to evaluate the stress fields on and below the contact surface, assuming a half space contact problem. The stress mean and amplitudes are then used to assess the fatigue damage according to a multi-axial fatigue criterion. In this study, the thermal behavior of the lubricated contact, which is commonly included for scuffing failure prediction [29, 31, 32], is excluded. It is also assumed there always exists a thin molecular boundary lubrication film within local asperity contact areas. The associated boundary lubrication friction coefficient is constant and independent from the starvation condition. The crack propagation after the nucleation of surface breaking crack is out of the scope of the current study. Using the model developed, a parametric simulation is performed to show fatigue life variations with starvation severity, surface roughness amplitude, lubricant viscosity (by varying lubricant temperature), and normal load. Therefore, in this study, efforts are devoted to the physical and computational description, and examination, of starved lubrication effect on surface crack nucleation for line contacts.

CHAPTER-2

THEORY AND FORMULATIONS

This section studies modeling methodology to evaluate fatigue life damage of spur gear. Governing formulations are considered to determine surface roughness, Lubrication film thickness, flow coefficient, viscosity, lubricant density parametric analysis conducted to know the effect of this properties film thickness in starved conditions. Surface parameters, lubricant properties, loads are considered to calculate near and below surface stresses. Multi-axial fatigue criterion was adopted to assess the Fatigue damage.

2.1 TRIBOLOGICAL BEHAVIOR

Line contact has been commonly used to represent contacts between spur gear teeth, whose crown along face width direction is limited and, therefore, tooth force density distribution is close to a uniform one. Defining *x* direction to be the one pointing into the direction of rolling and sliding, the hydrodynamic lubrication fluid flow bounded between solid surfaces 1 and 2, who move at respective velocities, u_1 and u_2, is described by the generalized Newtonian Reynolds equation as [29]

$$\frac{\partial}{\partial x}\left(\emptyset\frac{\partial p}{\partial x}\right) = u_r\,\frac{\partial(\theta\rho h)}{\partial x} + \frac{\partial(\theta\rho h)}{\partial t} \tag{2.1}$$

where *p* denotes pressure, *h* represents thickness of lubrication film, and u_r is usually referred as rolling velocity or entraining velocity, taking the average of the tangential velocities of the solid surfaces as $u_r = (u_1 + u_2)/2$.

The lubricant compressibility is included in Eq. (2.1) through the relationship between lubricant density, ρ, and pressure [9, 10]

$$\rho = \rho_0 \frac{1+\lambda_1 p}{1+\lambda_2 p} \tag{2.2}$$

Where λ_1= 2.266 GPa^{-1}, λ_2 = 1.683 GPa^{-1}, and ρ_0 is fluid density under ambient pressure. The second term on the right-hand side of Eq. (2.1) is a squeeze term and is dependent on time (t). The implementation of which allows the incorporation of transient effect introduced by moving surface roughness profiles. According to Elrod [30], a fluid film fraction parameter, θ , is used in Eq. (2.1) to describe lubrication starvation/cavitation. Taking the value between 0 and 1, θ indicates the extent of starvation/cavitation. When the gap between contacting surfaces is filled fully with pressurized hydrodynamic fluid,θ=1, indicating fully flooded lubrication condition. On the contrary, when the gap is filled proportionally with lubricant and air, θ<1, exhibiting a pressure that is lower than the ambient one and signifying lubrication is starved, or local cavitation takes place.

As gears rotate in mesh, the contact moves from start-of-active-profile to tip of the driving gear. Although sliding is small in the vicinity of pitch line, it is not the case for mesh positions far away from pitch line in addendum or dedendum area. In this latter circumstance, sliding is significant, and the lubricant non-Newtonian behavior is expected to decrease the lubrication film thickness [33].

This shear-thinning effect is included in the generalized Newtonian Reynolds equation through parameter ϕ, which is referred as the flow coefficient and has the form of [29]

$$\emptyset = \frac{\rho h^3}{\eta}\frac{1}{\hat{p}_x}\int_{-1/2}^{1/2}\hat{z}\hat{\tau}f(\hat{\tau})d\hat{z} \tag{2.3}$$

Where $\hat{P}_x = (h/G)(\partial p/\partial x)$, representing rolling direction pressure gradient. This dimensionless parameter is normalized utilizing film thickness, h, and lubricant Newtonian limit shear stress, G. Denoting an axis, which directs across the film thickness from surface 1 to surface 2, as z, its dimensionless counterpart, $\hat{z}$, used in Eq. (2.3), is defined as

$\hat{z} = z/h$ The origin of the $\hat{z}$ axis is set at the middle along the film thickness, and $\hat{z}$ = -1/2 and $1/2$ at surfaces 1 and 2, respectively. The lubricant low-shear viscosity, η, in Eq. (2.3), is experimentally characterized and found to be dependent on pressure and temperature as [34]

$$\eta = \eta_0\left(1+\frac{\hat{\alpha}}{\hat{b}}p\right)exp\left(\frac{C_F p}{p_\infty - p}\right) \tag{2.4}$$

where η_o is low-shear viscosity under ambient pressure, $\hat{\alpha}=a_0-a_1/T_f+a_2/T_f^2$,

$\hat{b} = b_o + b_1/T_f$ and $p_\infty = C_0+C_1/T_f$, all of which are functions of fluid temperature, T_f. The other constant C_F is a material parameter. Lastly, in Eq. (2.3), $f(\hat{\tau})$ is a lubricant rheological function that has the form of [33, 35].

$$f(\hat{\tau}) = \left(1+|\hat{\tau}|^{\beta}\right)^{\frac{1-n}{\beta n}} \tag{2.5}$$

where $\hat{\tau}$ is dimensionless viscous shear, and $\hat{\tau} = \tau/G$. The two constants involved in Eq. (5), n and β, are the shear rate sensitivity coefficient and the Yasuda parameter.

They are material properties and, similar to the other constants involved in Eq. (2.4), are obtained through experimental measurements [33-35].

Due to significant roughness profiles present on gear tooth surfaces produced by finishing processes, lubrication film is often not sufficiently thick to fully separate the mating surfaces for automotive gearing applications even under fully flooded lubrication condition. When starvation is concerned, local asperity contacts are expected to be much more frequent. To describe such contacts, the film thickness within the asperity interaction areas is constant, such that the film thickness gradient in the rolling direction is [16, 29].

$$\frac{\partial h}{\partial x} = 0 \tag{2.6}$$

It is noted the surface curvature gap before loading, g_0, and elastic deformation under loading, V [36], together with the roughness height fluctuations of surface 1, s_1, and surface 2, s_2, are included in the above governing equations via the film thickness description of $h = h_0 + g_0 - V - s_1 - s_2$ [16, 29]. Here, h_0 is a reference film thickness and is determined by implementing the equilibrium between applied normal force density, W, and contact pressure as.

$$\mathrm{W} = \int p dx \tag{2.7}$$

The numerical solution of the above tribological governing equations yields the normal contact pressure and film thickness distributions across the lubricated contact zone.

With which, the surface tangential shear stress is determined as $q = \eta\dot{\gamma}/f(\hat{\tau})$ for fluid areas, where $\dot{\gamma}$ is shear strain rate; and q = μ_bp for asperity contact areas, where boundary lubrication is assumed and the boundary lubrication friction coefficient, μ_b, is set to take the value of μ_b=0.1 , following Refs. [5, 6, 29]. The normal and tangential tractions, namely p and q, dictate the stress fields on and below the contact surface as described below.

2.2 Multi-axial Stress Fields

In view of the contact zone size, it is small in comparison to the contact body. Therefore, the half space assumption is employed, and the stress fields along the contact surface follow [36].

$$\sigma_x = -p(x,t) - \frac{2}{\pi}\int \frac{q(x',t)}{x-x'}dx' \tag{2.8a}$$

$$\sigma_y = -p(x,t) \tag{2.8b}$$

$$\sigma_{xy} = -q(x,t) \tag{2.8c}$$

Below the surface, the stress fields read [36]

$$\sigma_x = -\frac{2y}{\pi}\int \frac{p(x',t)(x-x')^2}{[(x-x')^2+y^2]^2}dx' - \frac{2}{\pi}\int \frac{q(x',t)(x-x')^3}{[(x-x')^2+y^2]^2}dx' \tag{2.9a}$$

$$\sigma_y = -\frac{2y^3}{\pi}\int \frac{p(x',t)}{[(x-x')^2+y^2]^2}dx' - \frac{2y^2}{\pi}\int \frac{q(x',t)(x-x')}{[(x-x')^2+y^2]^2}dx' \tag{2.9b}$$

$$\sigma_{xy} = -\frac{2y^2}{\pi}\int \frac{p(x',t)(x-x')}{[(x-x')^2+y^2]^2}dx' - \frac{2y}{\pi}\int \frac{q(x',t)(x-x')^2}{[(x-x')^2+y^2]^2}dx' \tag{2.9c}$$

In Eqs. (2.8) and (2.9), the *y* axis points downward from the surface into the material, and the integrals are performed over the entire contact zone. Considering a line contact with large width, which is representative for gear contacts, equations (2.8) and (2.9) assume plane strain condition.

It is also noted that surface topography effect is not included in the above stress formulations [37], since the half space adopted is perfectly smooth [36]. The surface roughness impact on stresses are included only through the normal and tangential tractions, *p* and *q*, yielded from the tribological analysis. To directly consider the surface topography variation in the stress field determination, the computationally much more involved boundary element method proposed by Li [37] may be used in the place of Eqs. (8) and (9), however, on the cost of significantly elevated computational efforts.

2.3 Fatigue Assessment

Provided the multi-axial stress fields from the section above, the stress amplitudes of normal and shear components, denoted as σ_a and τ_a respectively, are determined and used to evaluate the fatigue damage according a failure criterion. Criteria designed for the assessment of fatigue damage accumulation are diverse in literature. For contact problems where compressive stresses dominate, critical plane-based failure methods [38-41], or Weibull model based one [42] were employed by different researchers [5, 13-15] to show surface or near surface crack nucleation.

In view of the agreements between model predictions and experimental measurements [5, 6, 8], the multi-axial method of [41].

$$\frac{1}{S_b(N_f)}\sqrt{\sigma_a^2 + \left[\frac{S_b(N_f)}{s_t(N_f)}\right]\tau_a^2} = \varsigma\left(1 - \frac{\sigma_{m,max}}{S_y}\right) \qquad 2.10$$

appeared to yield better results, and thus is employed in this study. In Eq. (2.10), S_b and S_t represent fatigue strength of polished small specimens operating under fully reversed bending and torsion conditions, respectively. Their quantitative dependence on number of cyclic loading, N_f, was obtained through experimental measurements [6].

The mean normal stress effect on fatigue damage is included through the right hand side of Eq. (2.10), where $\sigma_{m,max}$ is the mean normal stress acting on the plane that experiences the maximum normal stress amplitude, S_y is the yield strength, and z is a material parameter that is dependent on the fatigue strength ratio of S_b/S_t [41].

CHAPTER-3

SIMULATIONS AND DISCUSSION

In this work, a line contact consisting of two cylinders, whose reduced radius of curvature $r` = 7.5$ μm and reduced elastic modulus E`=226 GPa, is employed. Two loading levels, namely W=637.5 N/mm and 835 N/mm, are employed to produce low and high Hertzian contact pressures as $p_h = 1.75$ GPa and 2.0 GPa, respectively. In order to investigate lubricant viscosity effect on contact fatigue under starved lubrication condition, two inlet lubricant temperatures are implemented as T_{in}= 100˚C and 50˚ C. Considering a Turbine fluid, MIL-L23699, its ambient low-shear viscosity, η_0, is increased from 4.64 mPas to 17.17 mPas when temperature is reduced from 100˚C to 50˚ C. The lubricant viscosity dependences on pressure, temperature, and shear rate were determined through experimental measurements [33-35]. As for speed condition of the contact, variation is excluded in this study. The rolling velocity is kept constant at u_r=10 m/s, and the sliding velocity that is defined as $u_s = u_1 - u_2$, is set at -5 m/s, resulting in a slide-to-roll ratio of $SR = u_s / u_r$. The negative u_s indicates surface 1 is moving slower than surface 2, representing the negative sliding condition that occurs in dedendum of driving gear of gear contacts, where pitting failure takes place.

To vary starvation extent, supplied inlet lubrication film thickness, h^{in} , is set to range from 0.2 μm to 10 μm. These low and high bounds selected for h^{in} correspond to severe starvation and no starvation conditions, respectively. Lastly, surface roughness effect is examined by using two roughness profiles measured from ground gear tooth surfaces along profile direction. As displayed in Figure.3.1, the smoother ground surface has the root-mean-square (RMS) roughness amplitude of R_q=0.3 μm, and the rougher one is characterized as R_q=0.5 μm. Summarized in Table.1, the above operating and surface conditions yield a total of 80 combinations, which are representative of typical automotive high-speed gearing applications that are subject to potential contact fatigue failure. It is noted that the values taken for h^{in} are slightly different for the two surface roughness profiles as listed in Table.1. This is for the purpose of a better description of the non-linear relationship between fatigue life and starvation under different roughness conditions. These h^{in} values are determined according to several tryouts. Defining the baseline simulation to be the smoother rough surface (R_q=0.3 μm) operates under the lower pressure ($p_h = 1.75$ GPa with W=637.5 N/m), lower viscosity

($\eta_0 = 4.64$ mPas at T_{in}=100˚C), and fully flooded (h^{in} =10 μm) condition, its tribological characteristics in terms of contact pressure, tangential shear, lubrication film thickness, and lubrication film fraction parameter are plotted in the left column of Figure.3.2. In the right column of the figure, the counterparts, where the inlet lubricant temperature is reduced to 50˚C,produce higher viscosity ($\eta_0 = 17.17$ mPas) while leaving the other parameters unchanged, are shown for comparison.

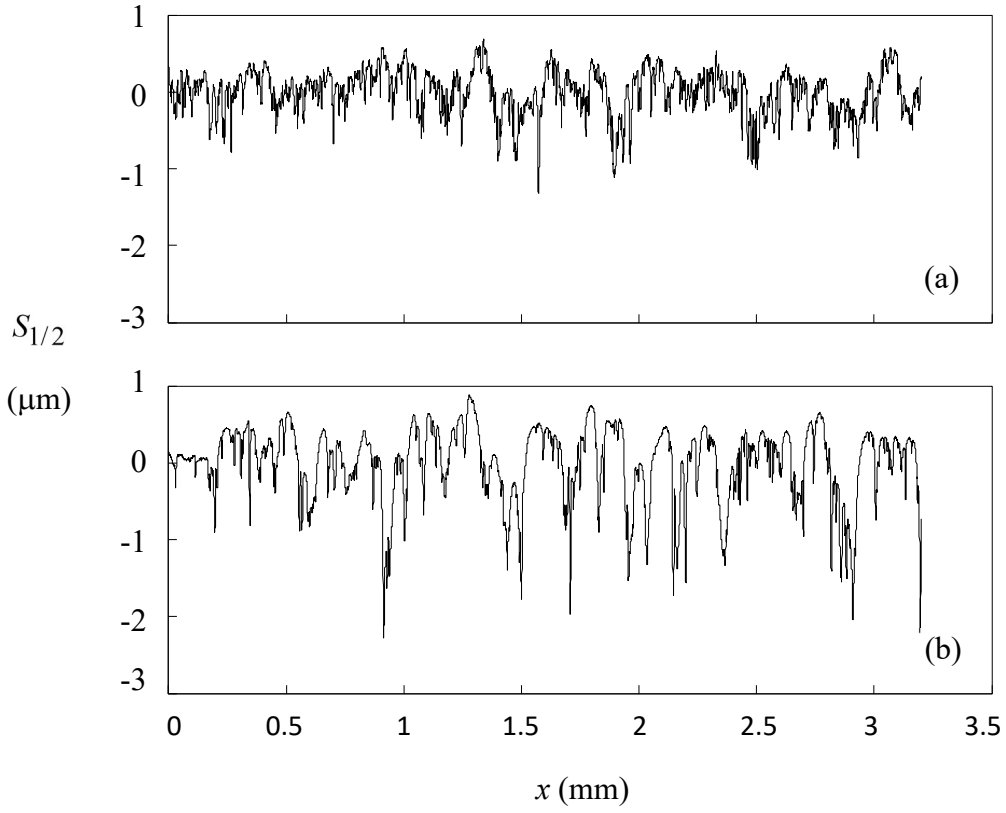

Figure.3.1 Measured surface roughness profiles of (a) R_q=0.3 μm , and (b) R_q=0.5 μm .

Table 1 Simulation matrix.

Hertzian Pressure, p_h, (GPa)		1.75, 2.0
Hertzian Half Width, a_h, (mm)		0.23, 0.27
Ambient Low-shear Viscosity, η_0, (mPas)		4.64, 17.17
Rolling Velocity, u_r, (m/s)		10
Slide-to-roll Ratio, *SR*		-0.5
RMS Roughness Amplitude, R_q (μm)		0.3, 0.5
Supplied Inlet Film Thickness, h^{in}, (μm)	R_q=0.3 μm	0.2, 0.4, 0.6, 1.0, 1.4, 1.8, 2.3, 3.0, 6.0, 10.0
	R_q=0.5 μm	0.2, 0.4, 0.6, 1.0, 1.8, 2.3, 3.0, 4.0, 6.0, 10.0

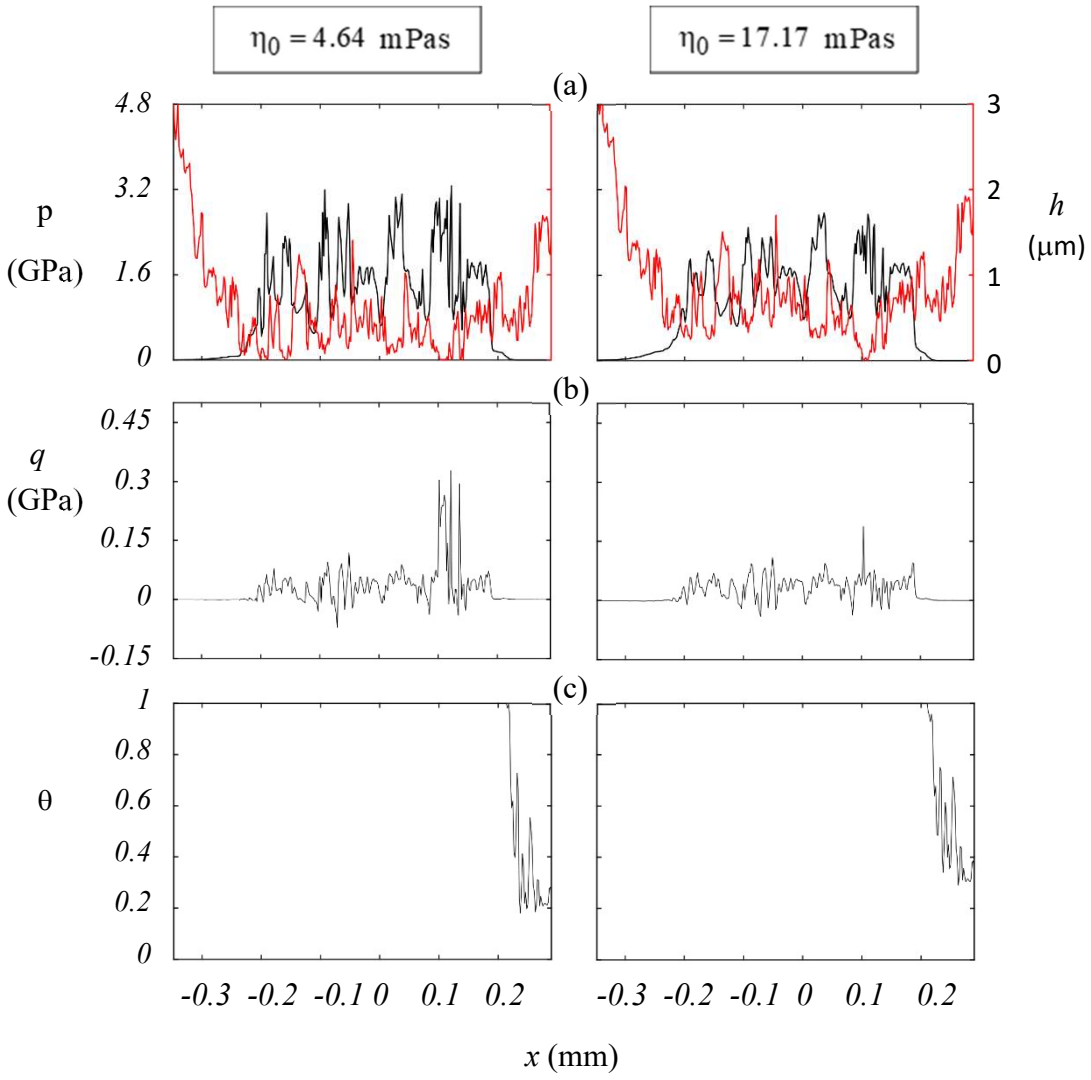

Figure.3.2 Transient distributions of (a) contact pressure (black) and lubrication film thickness (red), (b) surface shear, and (c) film fraction parameter for surface of R_q=0.3 μm operating under $p_h = 1.75$ GPa and $h^{in} = 10$ μm.

It is as expected that the film thickness increases with the increase of the lubricant viscosity. Consequently, the normal pressure and tangential shear are effectively decreased. In the last row of Figure.3.2, θ=1 in the vicinity of the inlet, indicating non-starved lubrication condition. It should be noted the tribological behavior as shown in Figure.3.2 is time-dependent due to the movement of the surface roughness profiles. As shown in Figure.3.23, both the maximum contact pressure, p_{max}, and the average film thickness within the nominal Hertzian zone, which is defined as $h_{avg} = \int_{-a_h}^{a_h} (\theta h) dx \Big/ (2a_h)$ with a_h representing the half Hertzian width, fluctuate with time largely. Considering this time period of Figure.3.23, the median maximum contact pressure, $\bar{p}_{max}$, and the median average film thickness, $\bar{h}_{max}$, are observed to decrease from 3.95 GPa to 3.29 GPa and increase from 0.386 μm to 0.603 μm, respectively, when the lubricant viscosity is raised from the baseline. The comparison behavior as those in figure.3.2 for other operating condition combinations defined in Table 1 are also constructed and illustrated below. From Figure.3.3- 3.22.

As the loaded contact pair rolls against each other, material points, p_i (i=1,M), at a certain depth, y, pass through the computational domain at the velocity u_1, for contact body 1, as illustrated in Figure.3.24. Owing to the time-varying contact pressure and tangential shear, each material point experiences different histories of multi-axial stress components. The associated fatigue damages and fatigue lives are, thus, different as well, although located at the same depth, and were observed to follow a normal distribution [5]. The median fatigue life of the material point population at depth y [p_i (i=1,M)], denoted as $\bar{N}_f$ is then used as a measure of the fatigue damage at the depth y. As shown in Figure.3.2, the pressure and shear peaks are significant for rough surface contacts, which lead to severe

near surface stress concentrations as depicted in Figure.3.25 at one example time instant under the baseline condition. The stress amplitudes are seen to reach maxima at the surface for the normal components. As for the shear stress, σ_{xy}, local maximum amplitudes appear at both the surface and the subsurface location at y =0.7 μm. This roughness induced near surface stress concentrations have been shown to be responsible for the surface breaking crack nucleation [5, 6, 8, 16]. In this study, the median fatigue life at the surface, $\bar{N}_{f0} = \bar{N}_f\big|_{y=0}$, is also found to be the minimum along the depth direction, and, therefore, used to represent the crack nucleation life.

For the 80 simulations defined in Table 1, the predicted crack nucleation fatigue lives are compared in Figure.3.26, where both axes are on $\log_{10}$ scale, showing the relationship between $\bar{N}_{f0}$ and h^{in}. The left and right columns of the figure represent the simulation results with surface roughness amplitudes of R_q =0.3μm and 0.5 μm, respectively; and the top and bottom rows correspond to the low and high loading conditions, respectively. For all the four roughness and load combinations, it is seen the fatigue life is not largely impacted initially as the supplied inlet lubrication film thickness decreases, until h^{in} reaches a sufficiently small value, which is referred as the first threshold, h_1^{in} (displayed for the curve under R_q =0.3μm, $p_h = 1.75$ GPa, and $\eta_0 = 4.64$ mPas). Below this first threshold, a sharp reduction in $\bar{N}_{f0}$ is initiated. However, this steep trend does not continue after h^{in} drops below a smaller second threshold, h_2^{in}(displayed for the same curve as for h_1^{in}). This behavior is in line with the experimental observation of Ref. [23]. The reason for such a non-linear relationship is explored utilizing Figure.3.7, where the median of Hertzian zone average film thickness, $\bar{h}_{avg}$ is plotted against h^{in}.

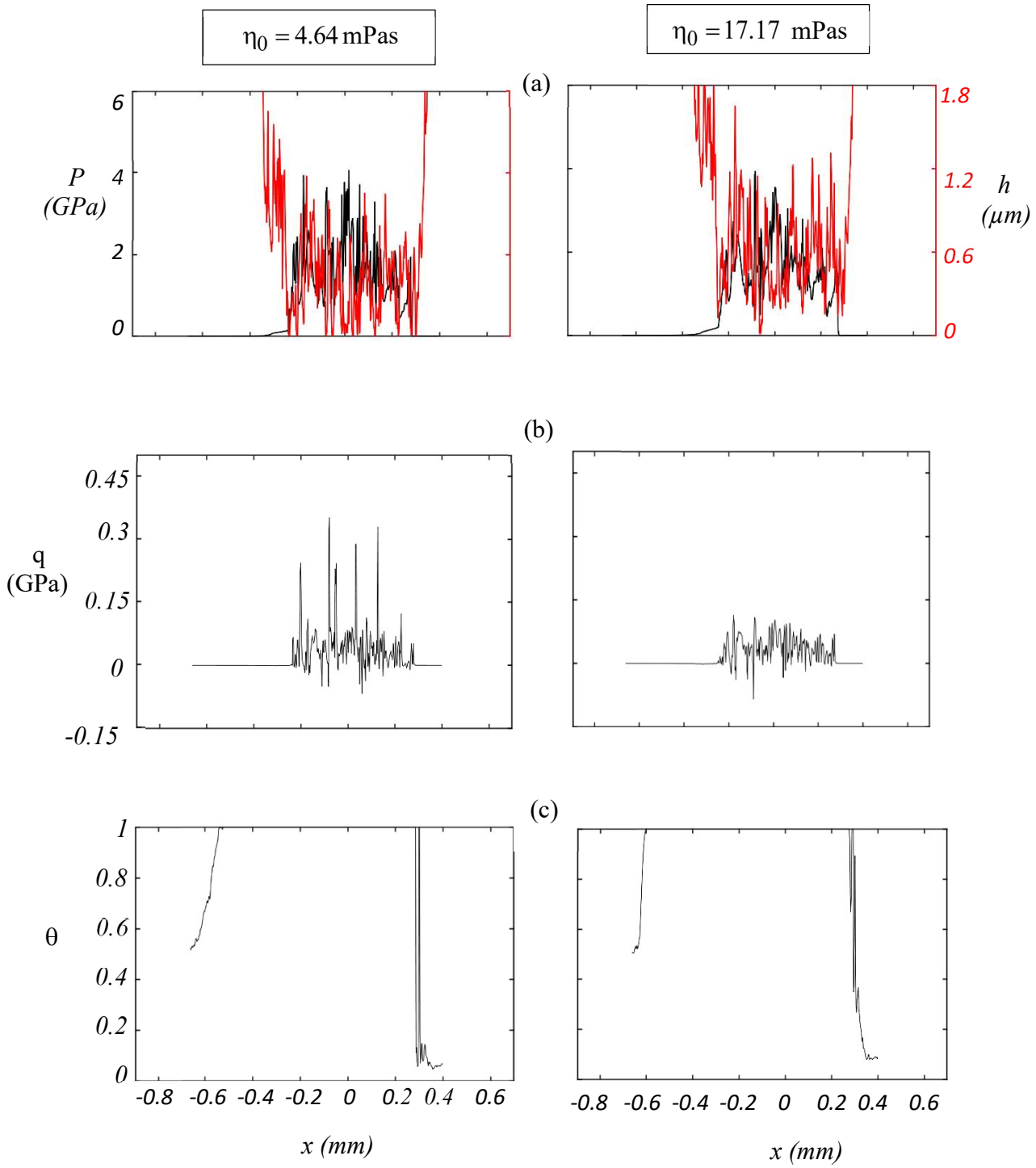

Figure.3.3 Initial distribution of (a) contact pressure (black) and lubrication film thickness(red), (b) surface shear, and (c) film fraction parameter for surface of R_q= 0.3 μm operating under P_h= 2 GPa and h^{in} = 0.2μm.

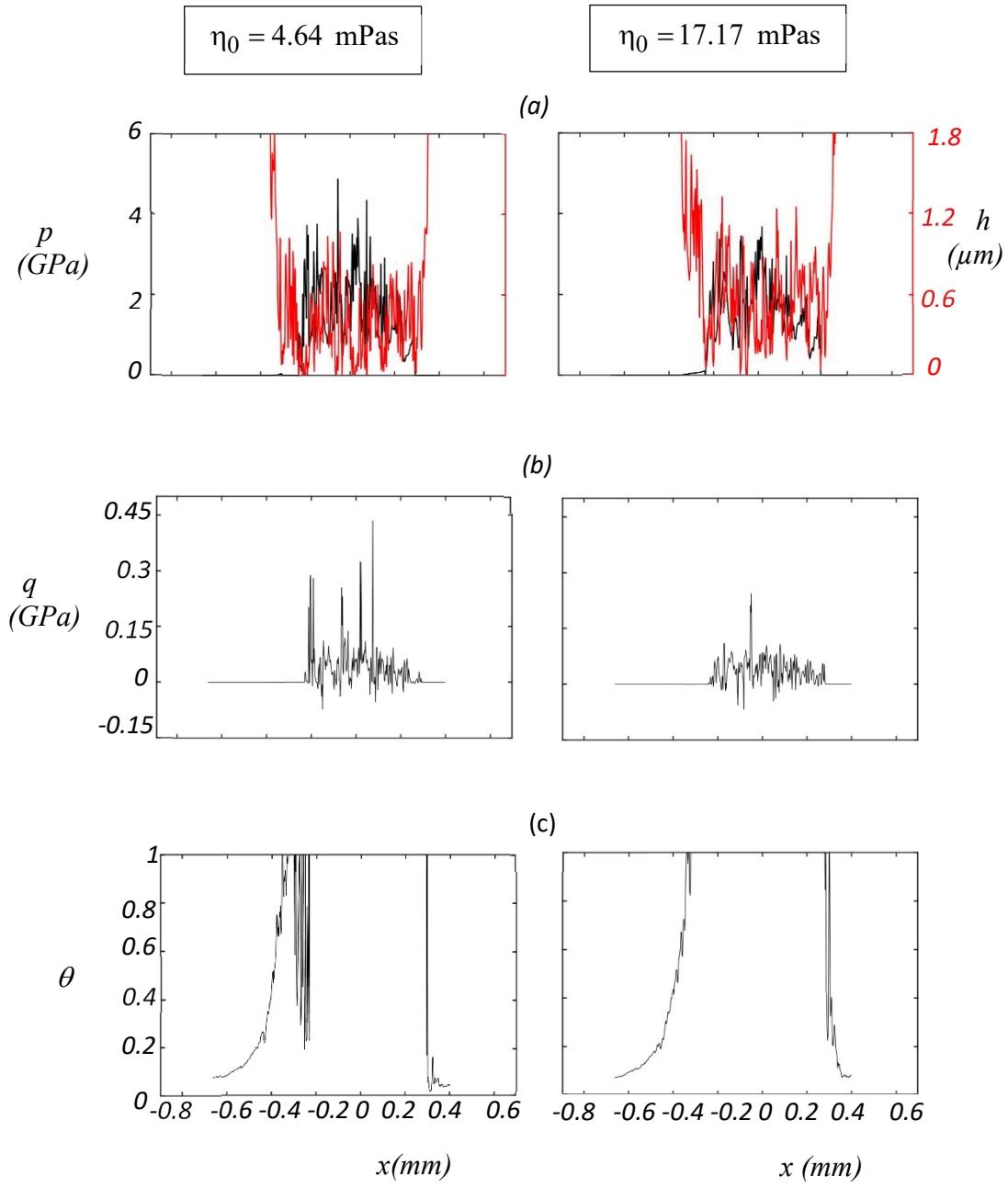

Figure.3.4 Transition distribution of (a) contact pressure (black) and lubrication film thickness (red), (b) surface shear, and (c) film fraction parameter for surface of R_q= 0.3 μm operating under p_h=2 GPa and h^{in} =1.8 μm

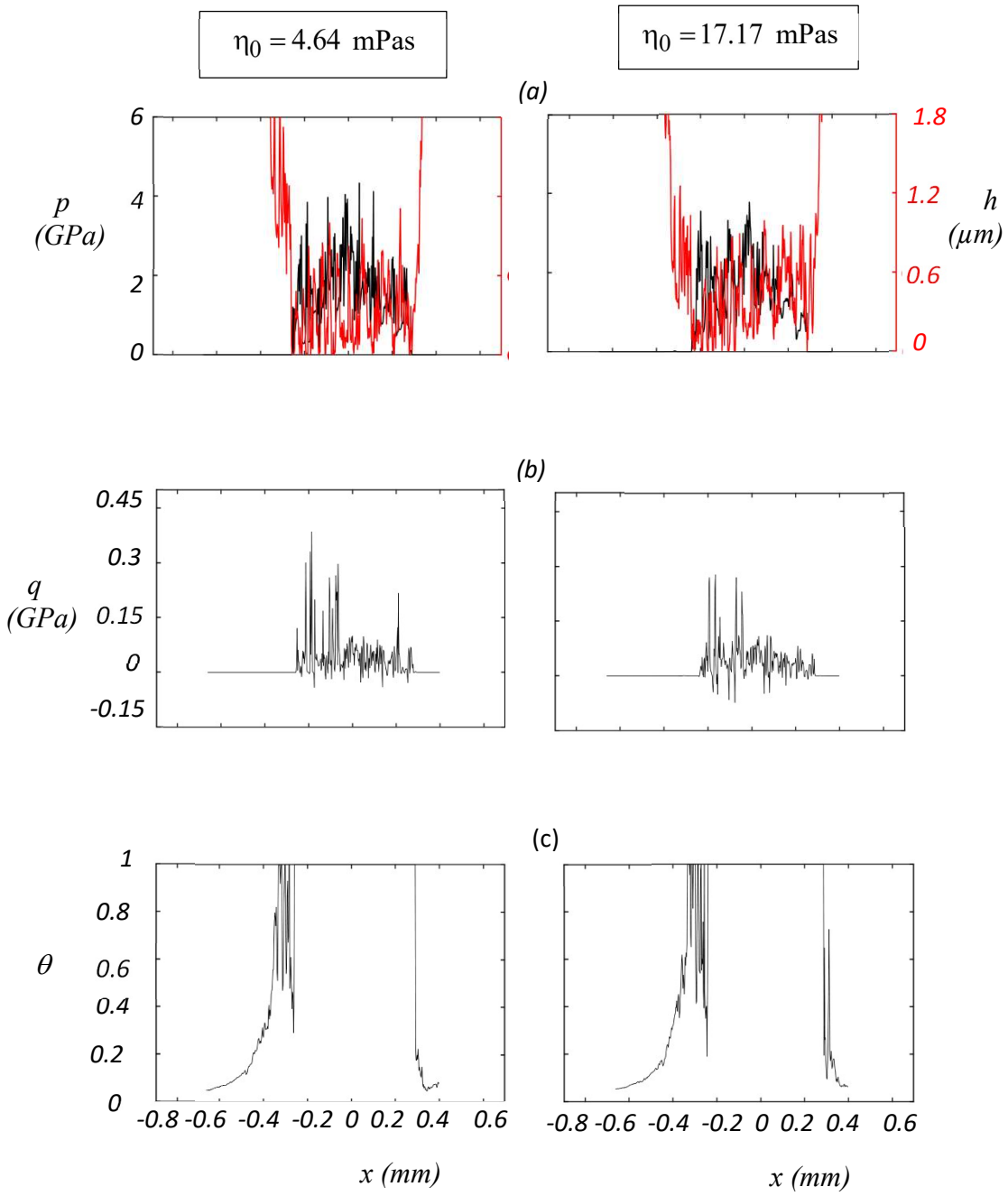

Figure.3.5 Transition distribution of (a) contact pressure (black) and lubrication film thickness (red), (b) surface shear, and (c) film fraction parameter for surface of R_q= 0.3 μm operating under p_h=2 GPa and h^{in}=2.3 μm

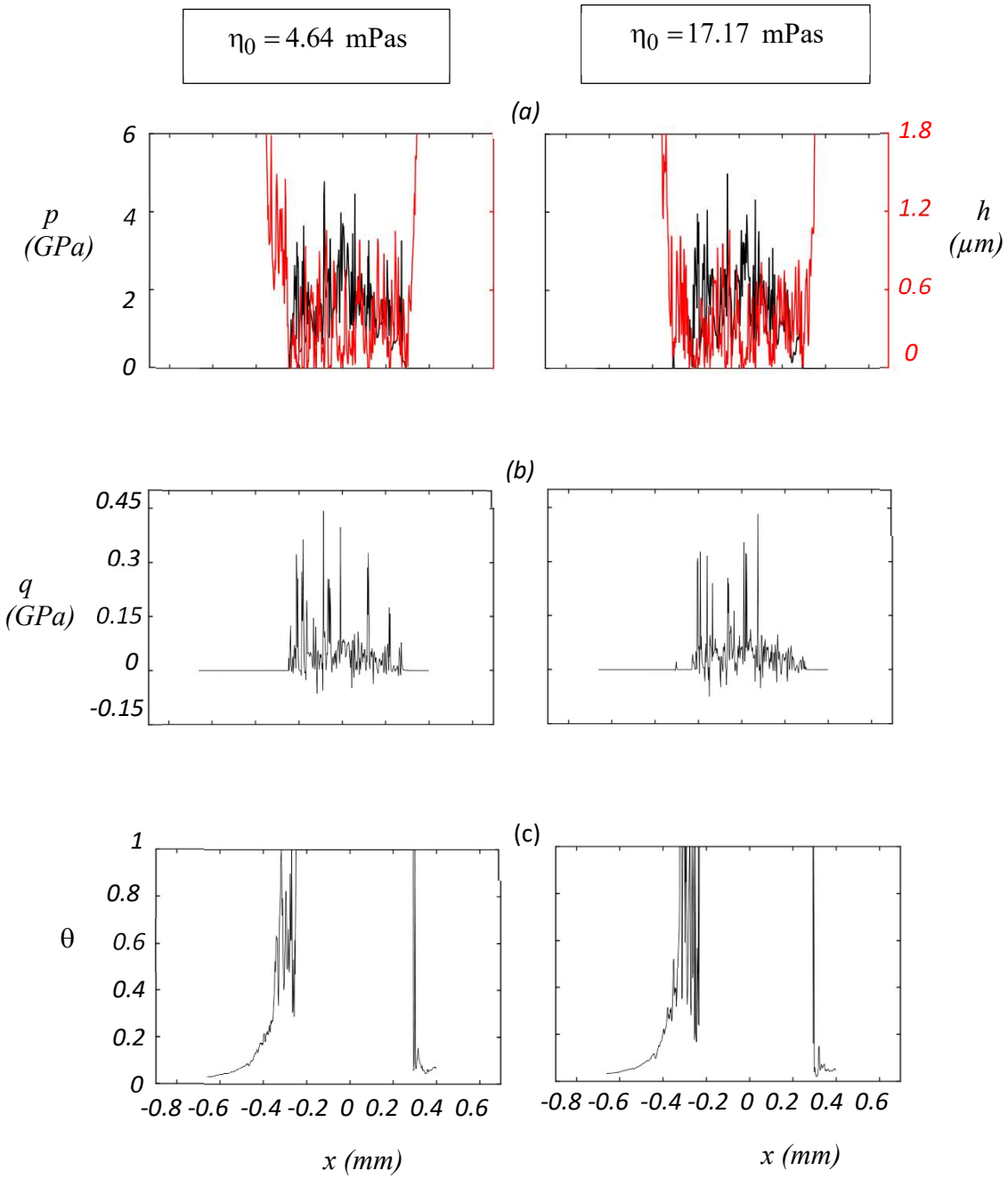

Figure.3.6 Transition distribution of (a) contact pressure (black) and lubrication film thickness (red), (b) surface shear, and (c) film fraction parameter for surface of R_q= 0.3 μm operating under p_h=2 GPa and h^{in}=3 μm

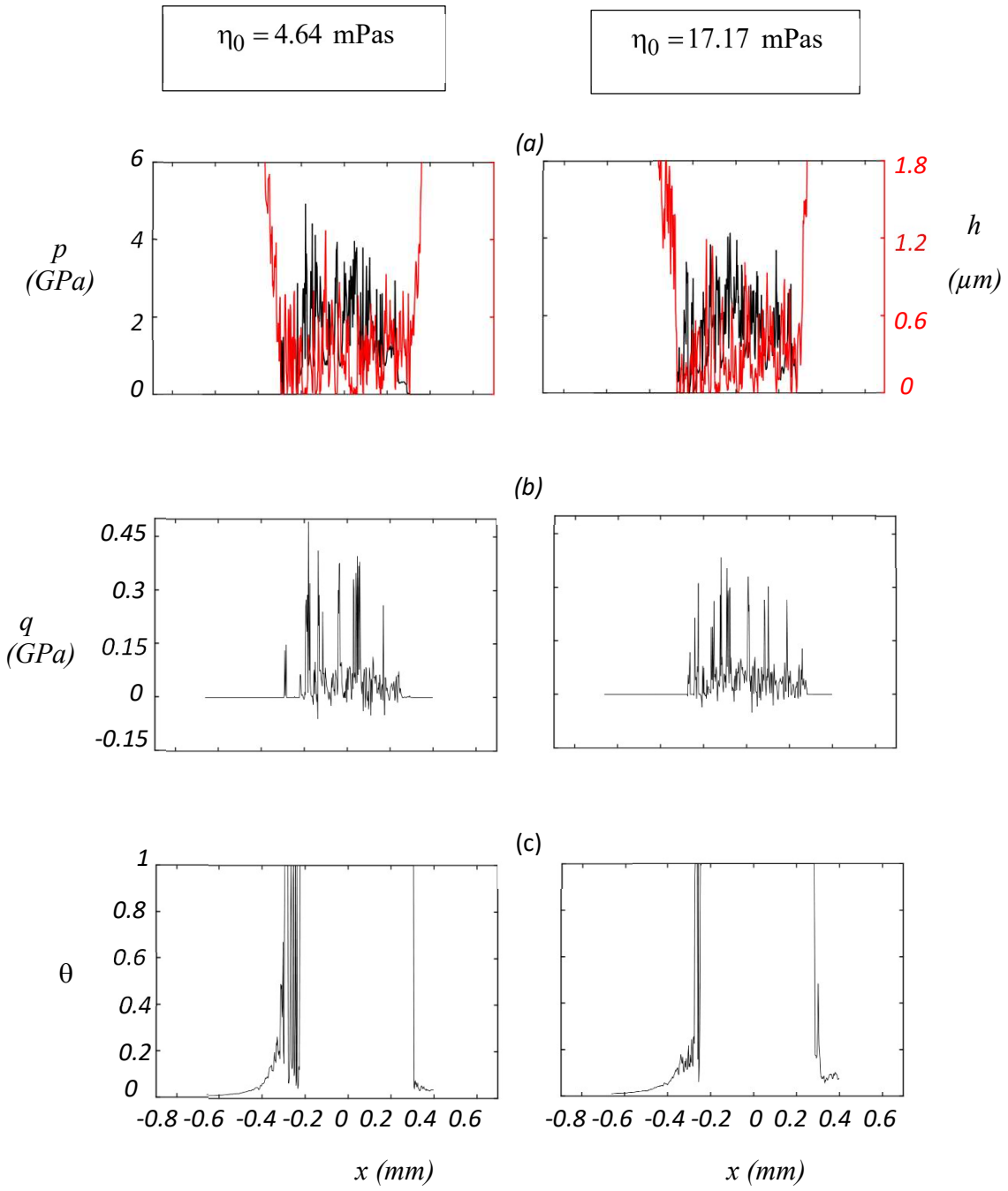

Figure.3.7 Final distribution of (a) contact pressure (black) and lubrication film thickness(red), (b) surface shear, and (c) film fraction parameter for surface of R_q= 0.3 μm operating under p_h=2 GPa and h^{in}= 10μm

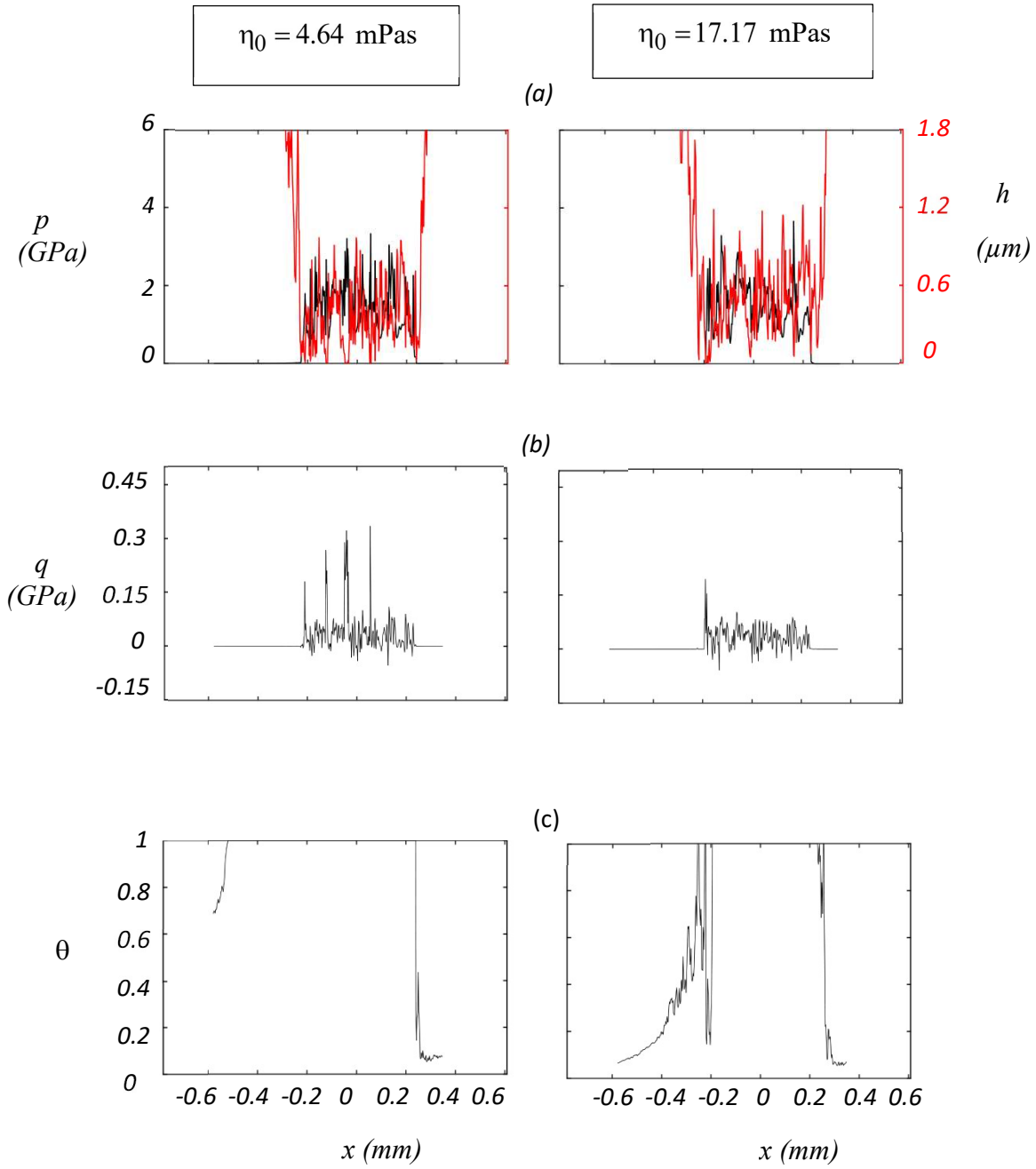

Figure3.8 Initial distribution of (a) contact pressure (black) and lubrication film thickness(red),(b) surface shear, and (c) film fraction parameter for surface of R_q= 0.3 μm operating under P_h= 1.75 GPa and h^{in}= 0.2μm

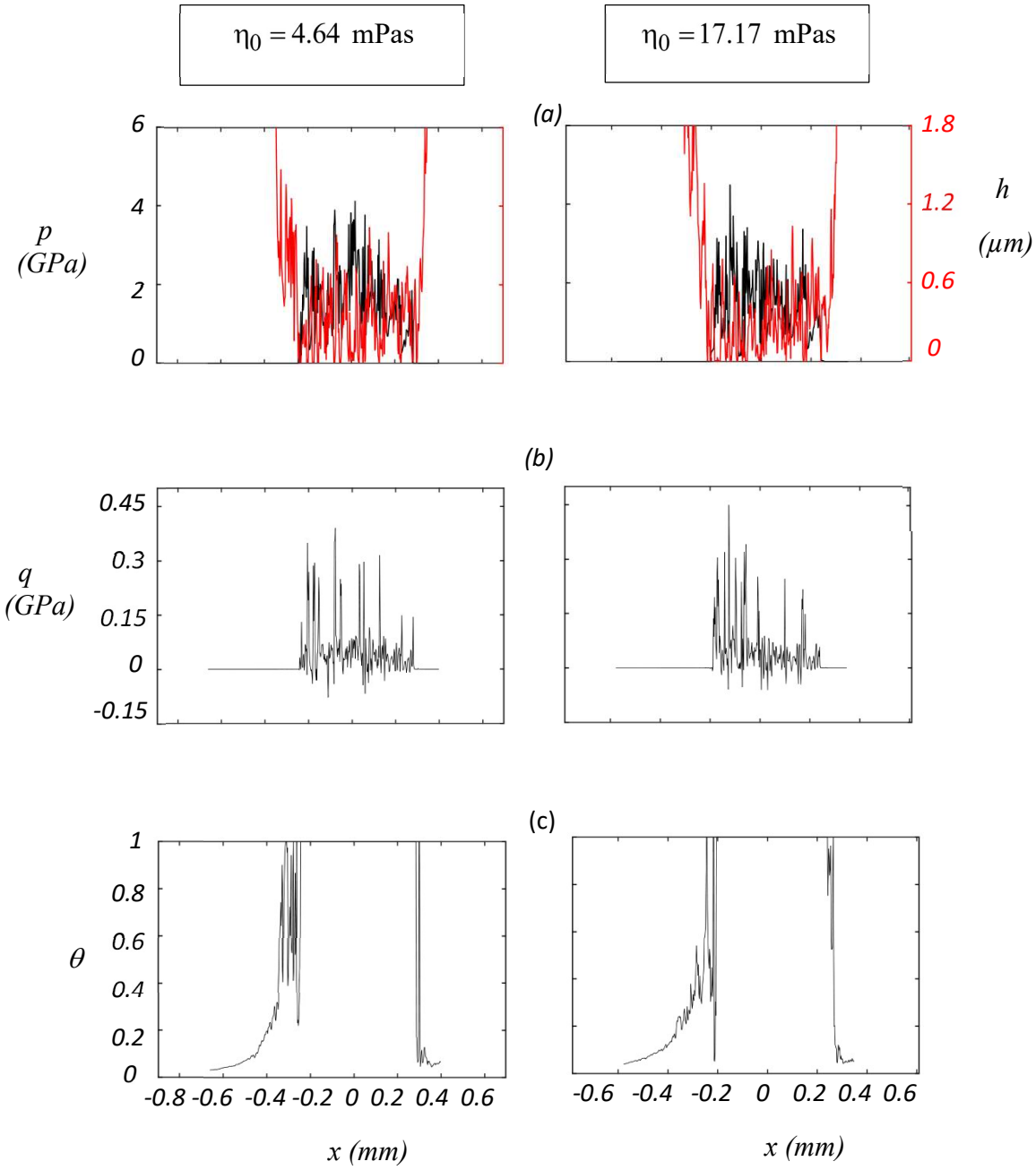

Figure.3.9 Transition distribution of (a) contact pressure (black) and lubrication film thickness(red), (b) surface shear, and (c) film fraction parameter for surface of R_q= 0.3 μm operating under P_h= 1.75 GPa and h^{in}= 1.8μm

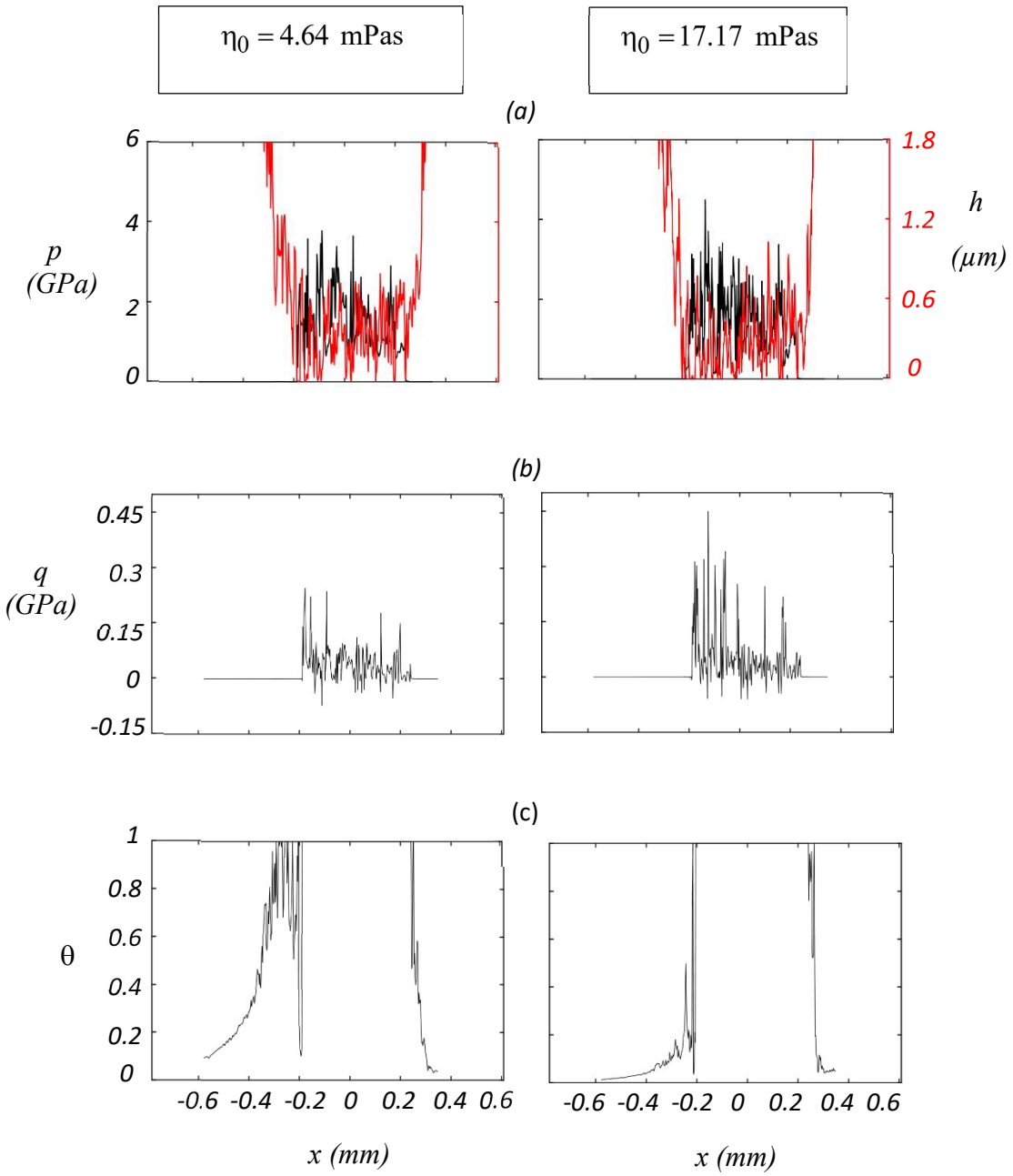

Figure.3.10 Transition distribution of (a) contact pressure (black) and lubrication film thickness(red), (b) surface shear, and (c) film fraction parameter for surface of R_q= 0.3 μm operating under P_h= 1.75 GPa and h^{in}= 2.3μm

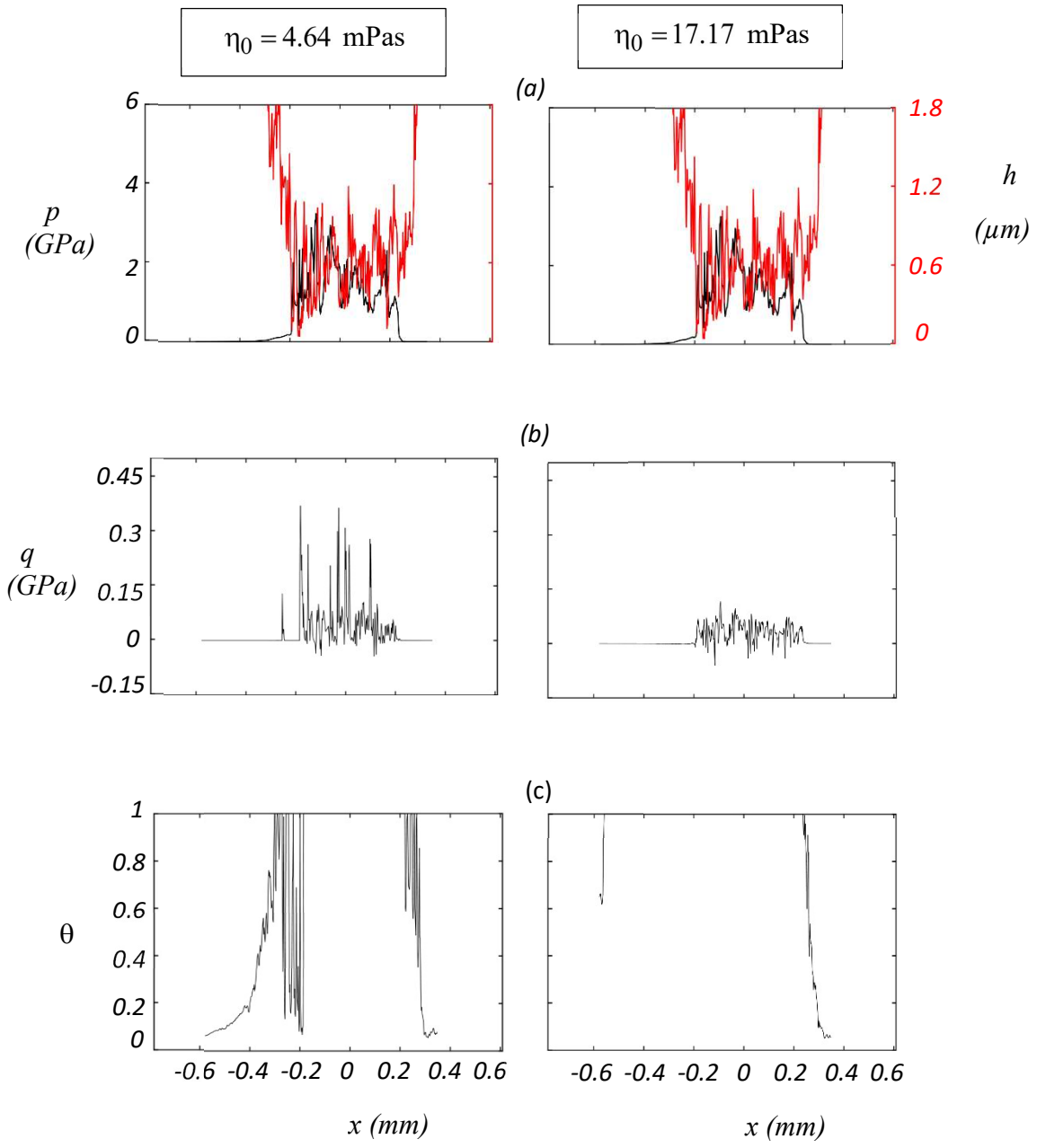

Figure3.11 Transition distribution of (a) contact pressure (black) and lubrication film thickness (red), (b) surface shear, and (c) film fraction parameter for surface of R_q= 0.3 μm operating under P_h= 1.75 GPa and h^{in}= 3μm.

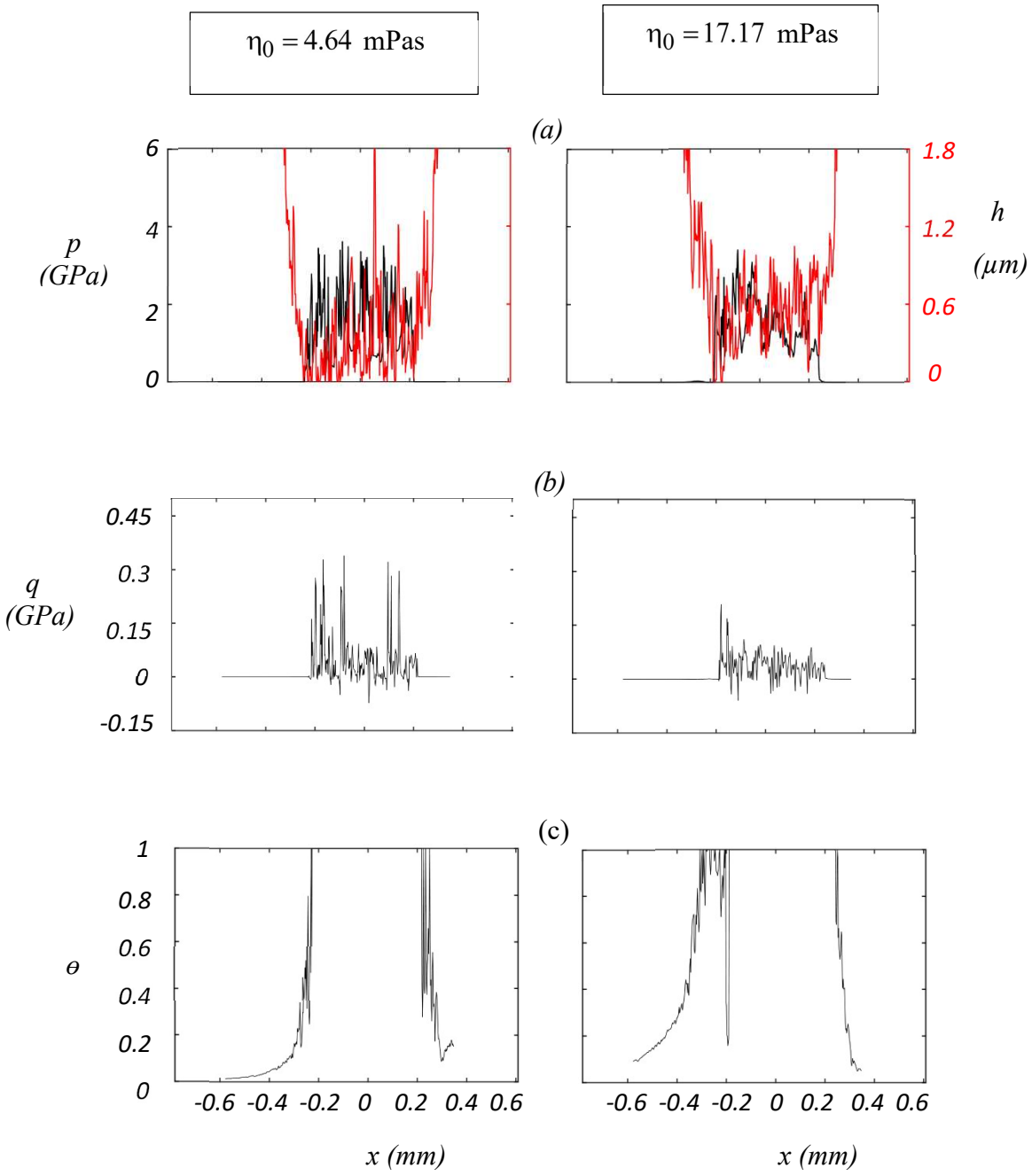

Figure.3.12 Final distribution of (a) contact pressure (black) and lubrication film thickness (red), (b) surface shear, and (c) film fraction parameter for surface of R_q= 0.3 μm operating under P_h= 1.75 GPa and h^{in}= 10μm.

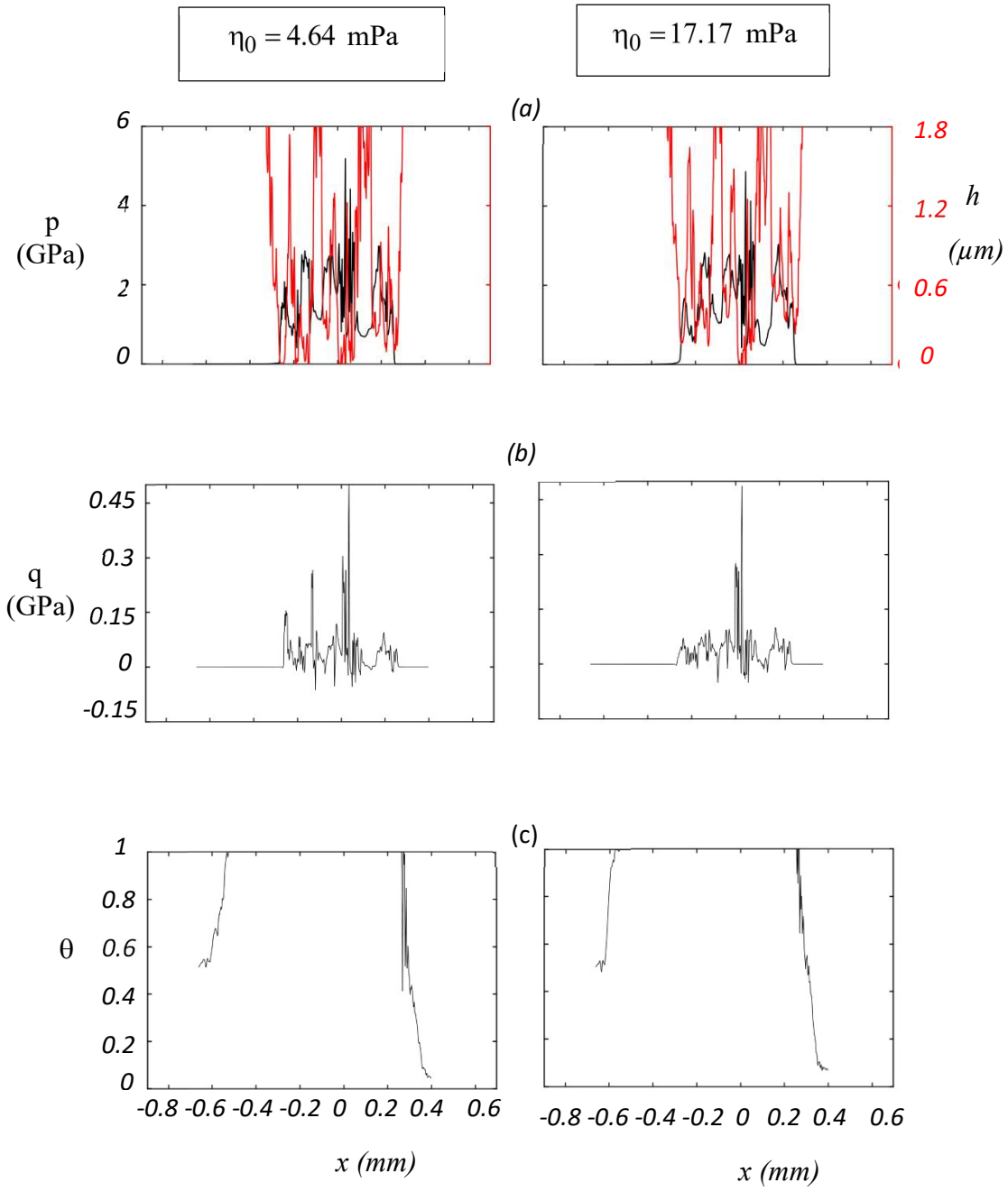

Figure.3.13 Initial distribution of (a) contact pressure (black) and lubrication film thickness (red), (b) surface shear, and (c) film fraction parameter for surface of $R_q = 0.5$ μm operating under $P_h = 2$ GPa and $h^{in} = 0.2$μm

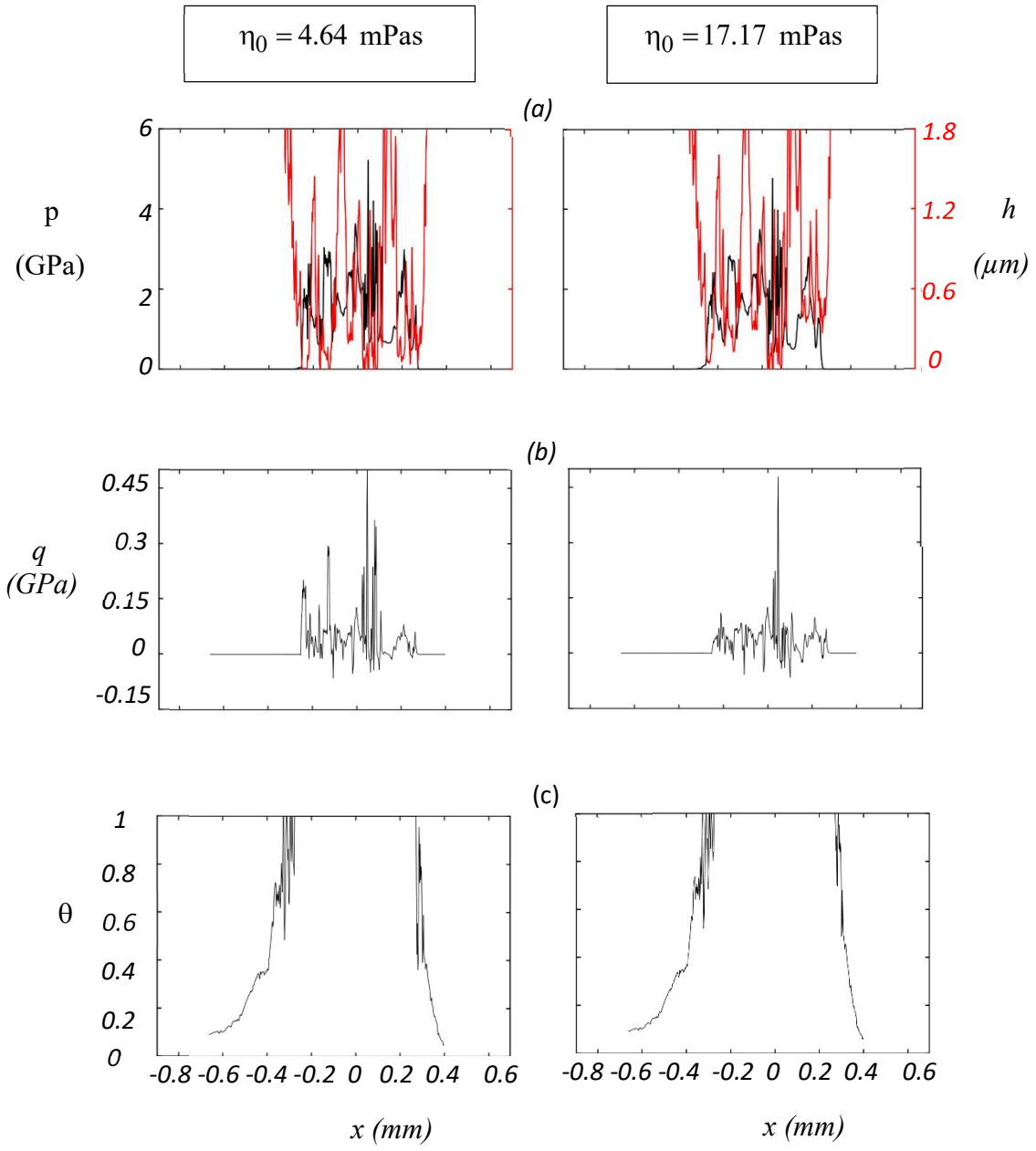

Figure.3.14 Transition distribution of (a) contact pressure (black) and lubrication film thickness (red), (b) surface shear, and (c) film fraction parameter for surface of R_q= 0.5 μm operating under P_h= 2GPa and h^{in}= 1.8μm.

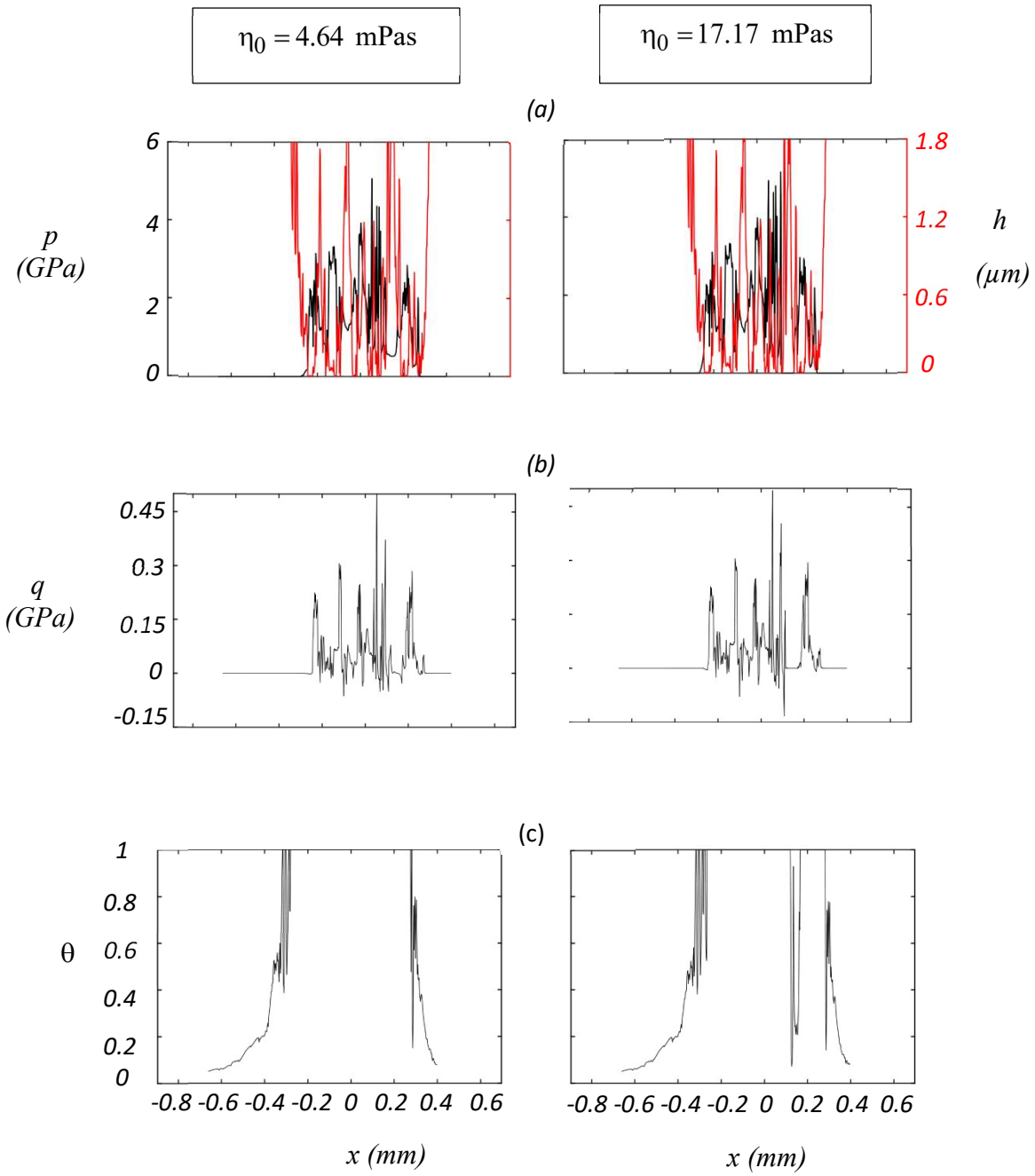

Figure3.15 Transition distribution of (a) contact pressure (black) and lubrication film thickness (red), (b) surface shear, and (c) film fraction parameter for surface of R_q= 0.5 μm operating under P_h= 2GPa and h^{in}= 2.3μm.

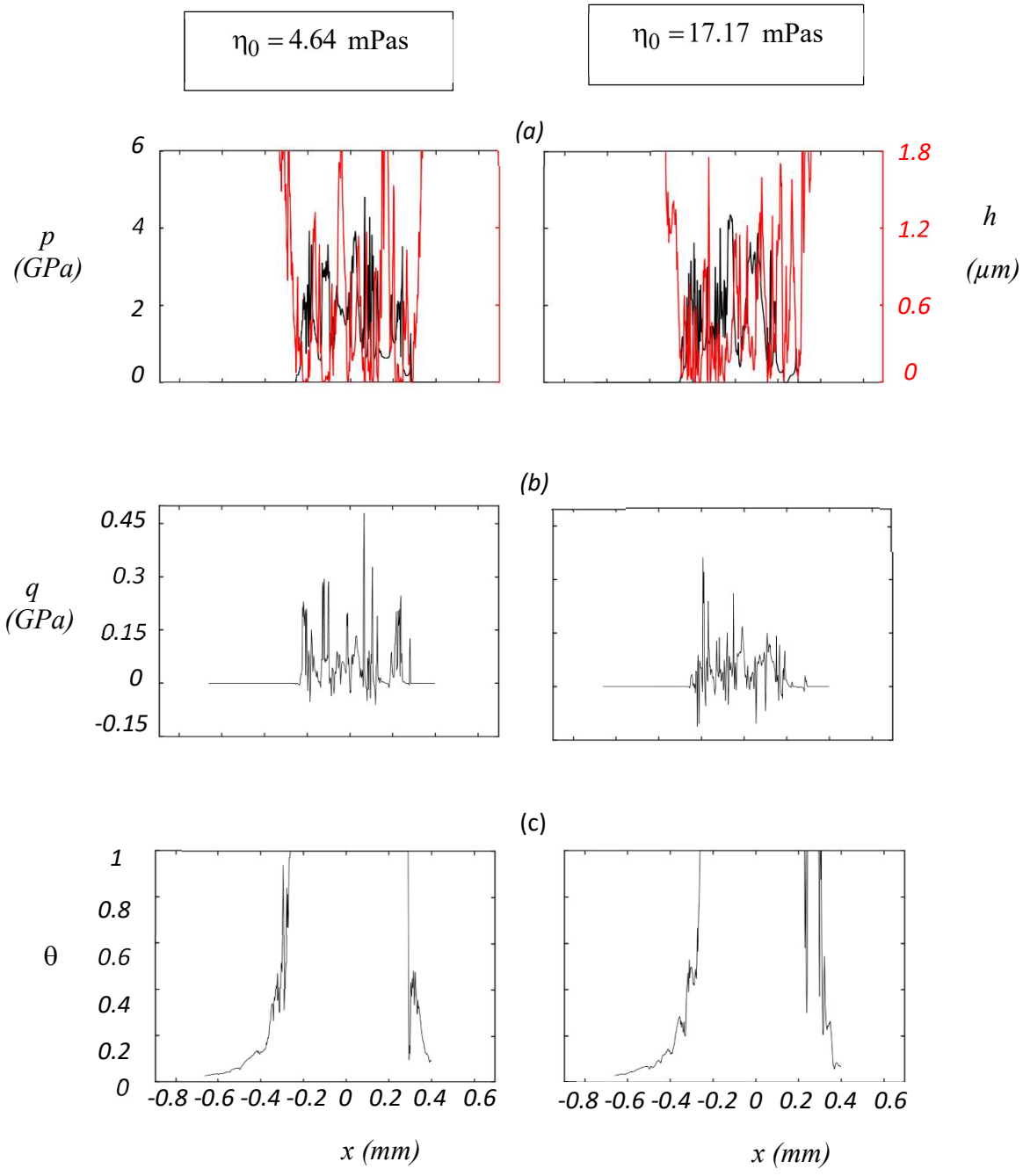

Figure.3.16 Transition distribution of (a) contact pressure (black) and lubrication film thickness (red), (b) surface shear, and (c) film fraction parameter for surface of R_q= 0.5 μm operating under P_h= 2 GPa and h^{in}= 3 μm.

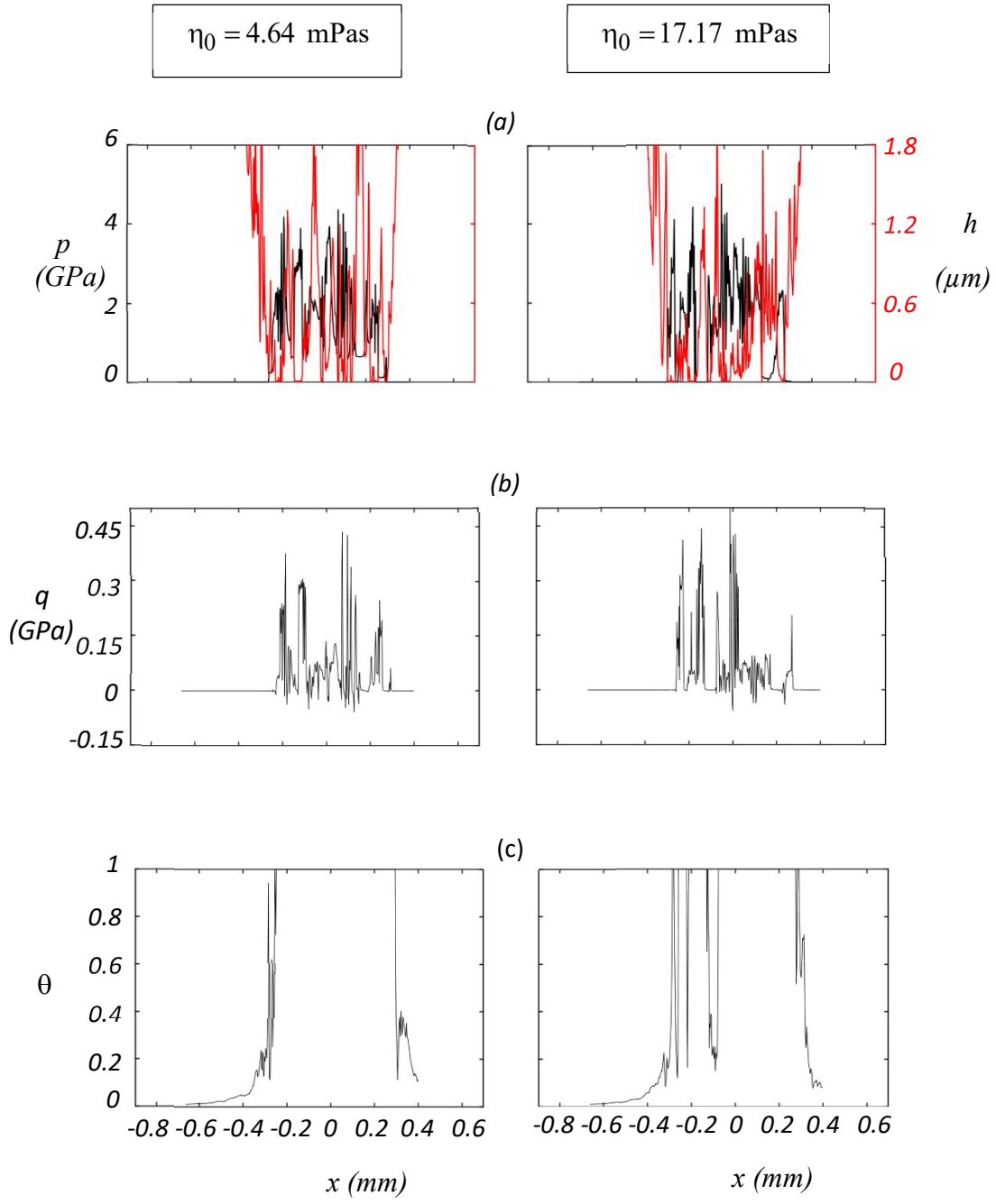

Figure.3.17 Final distribution of (a) contact pressure (black) and lubrication film thickness (red), (b) surface shear, and (c) film fraction parameter for surface of R_q= 0.5 μm operating under P_h= 2GPa and h^{in}= 10 μm.

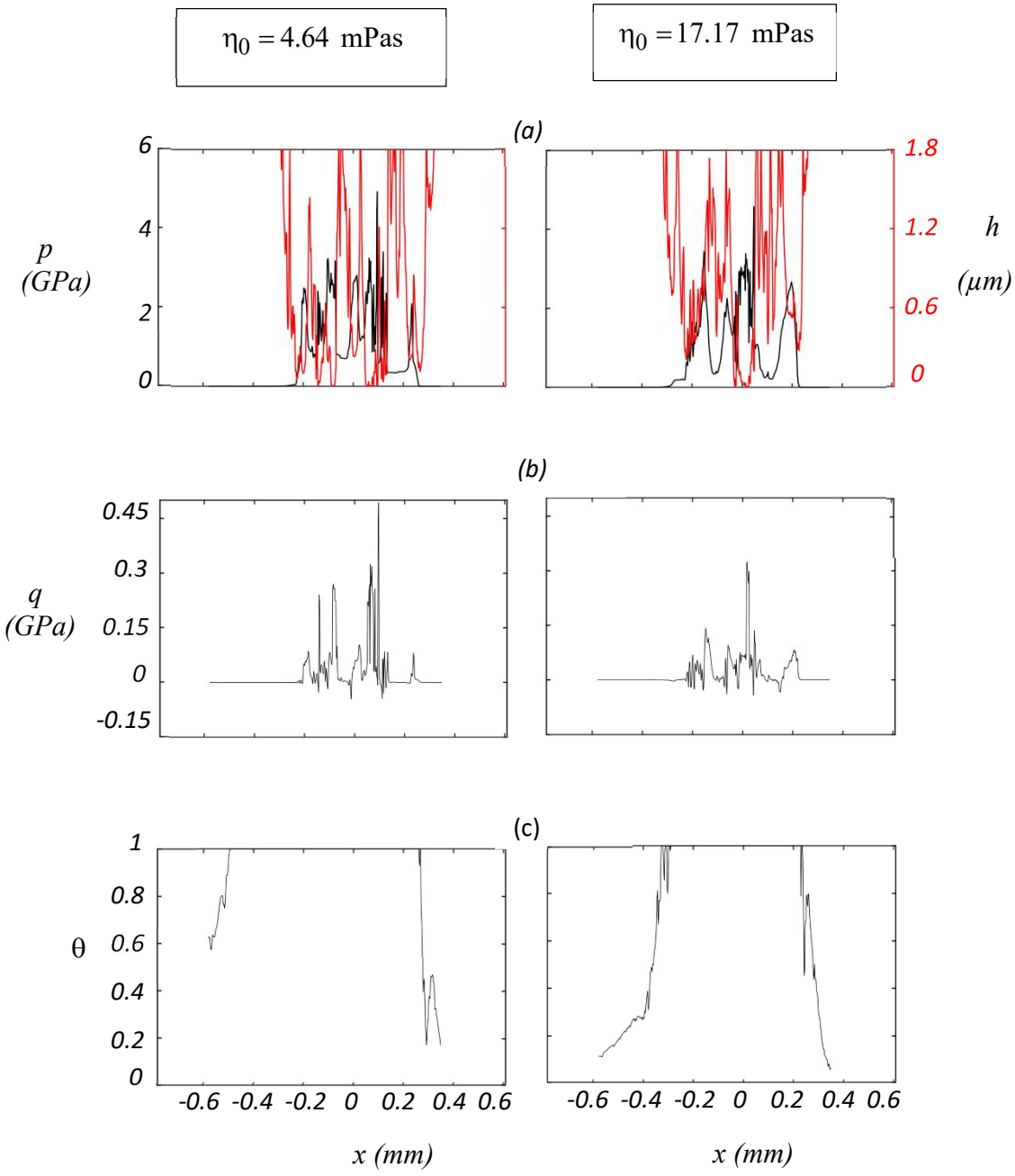

Figure.3.18 Initial distribution of (a) contact pressure (black) and lubrication film thickness (red), (b) surface shear, and (c) film fraction parameter for surface of R_q= 0.5 μm operating under P_h= 1.75 GPa and h^{in}= 0.2 μm.

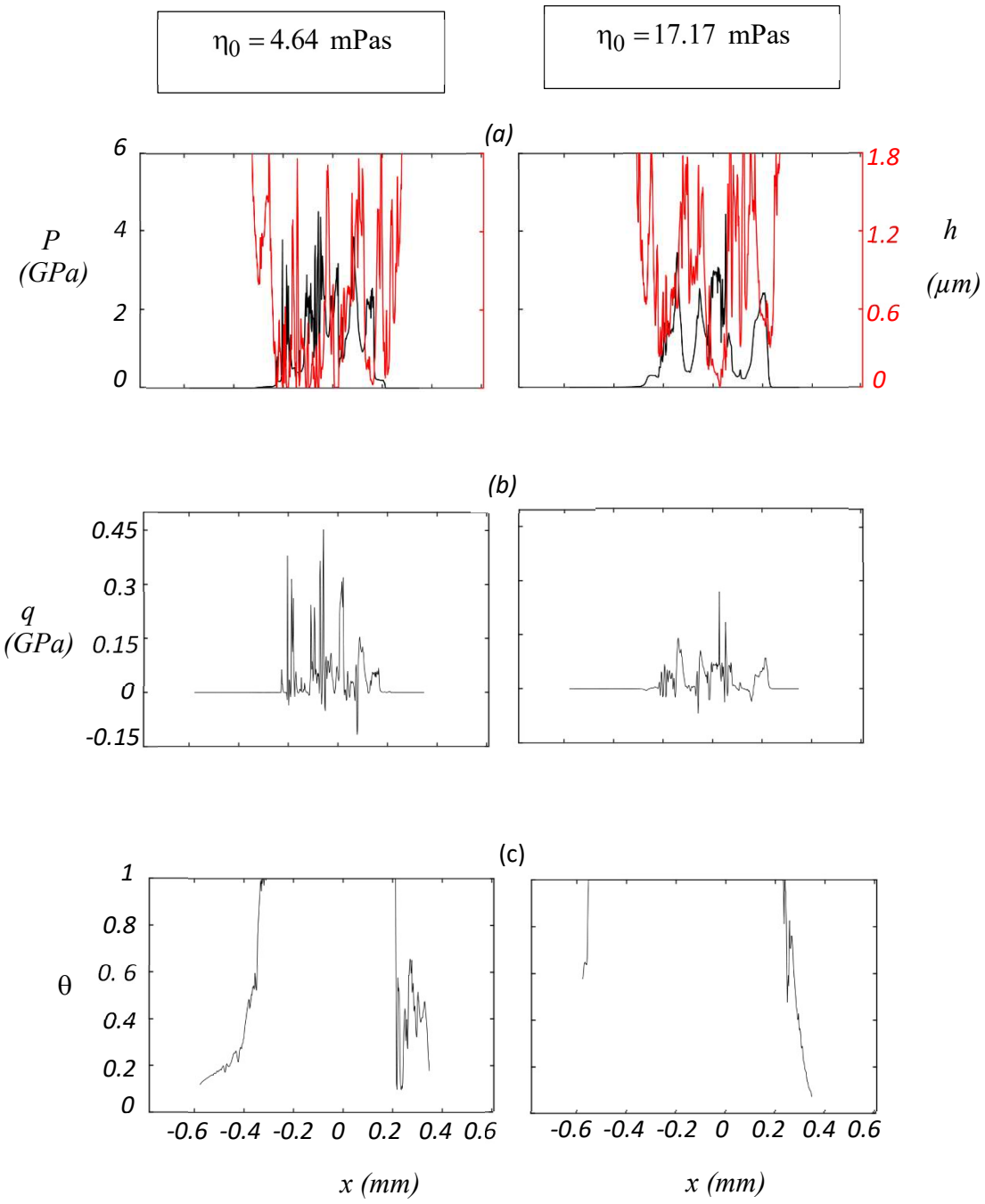

Figure.3.19 Transition distribution of (a) contact pressure (black) and lubrication film thickness (red), (b) surface shear, and (c) film fraction parameter for surface of R_q= 0.5 µm operating under P_h= 1.75 GPa and h^{in}= 1.8 µm.

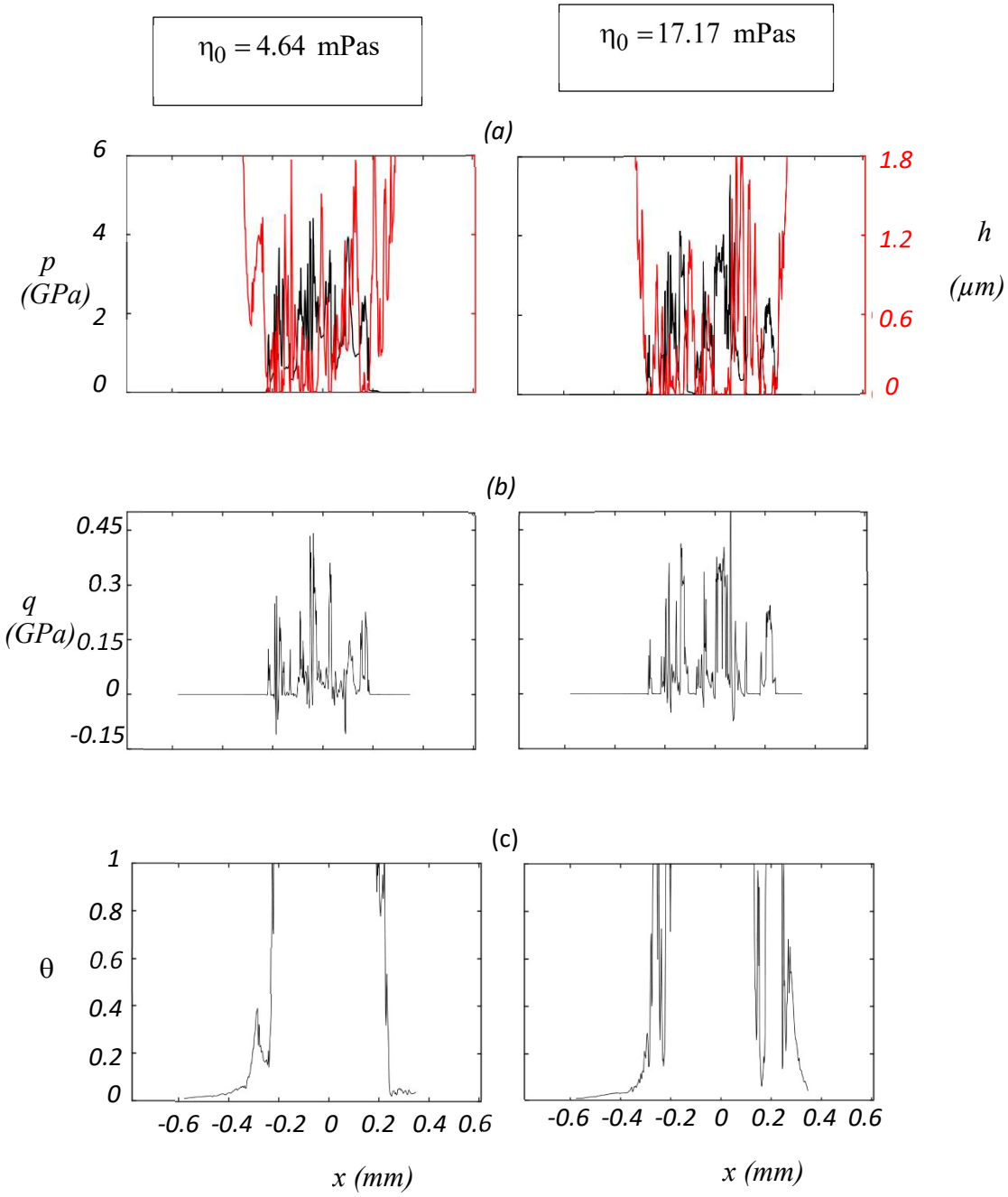

Figure.3.20 Transition distribution of (a) contact pressure (black) and lubrication film thickness (red), (b) surface shear, and (c) film fraction parameter for surface of R_q= 0.5 μm operating under P_h= 1.75 GPa and h^{in}= 2.3 μm

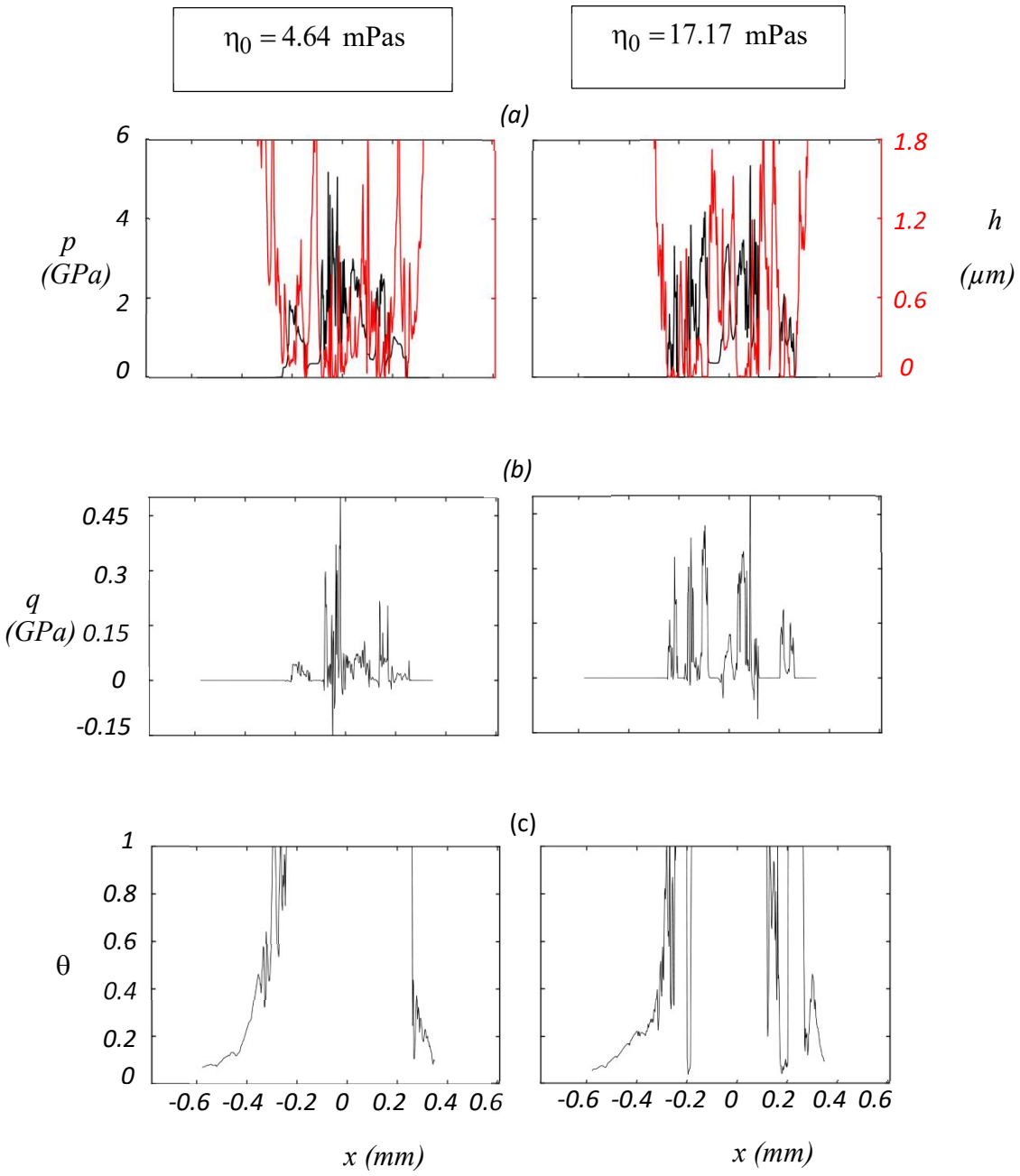

Figure.3.21 Transition distribution of (a) contact pressure (black) and lubrication film thickness (red), (b) surface shear, and (c) film fraction parameter for surface of R_q= 0.5 μm operating under P_h= 1.75 GPa and h^{in} = 3 μm

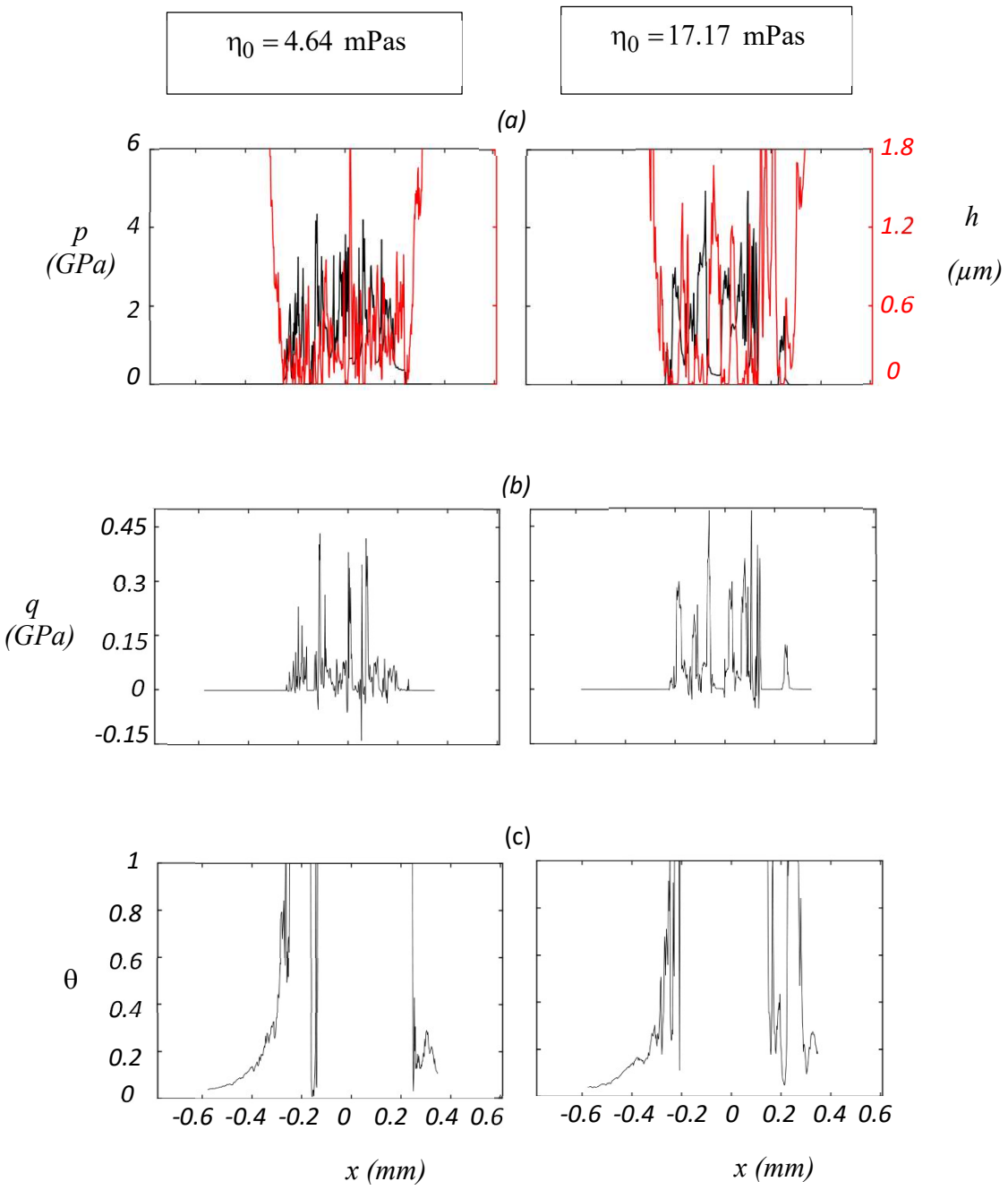

Figure.3.22 Final distribution of (a) contact pressure (black) and lubrication film thickness (red), (b) surface shear, and (c) film fraction parameter for surface of R_q= 0.5 μm operating under P_h= 1.75 GPa and h^{in}= 10 μm

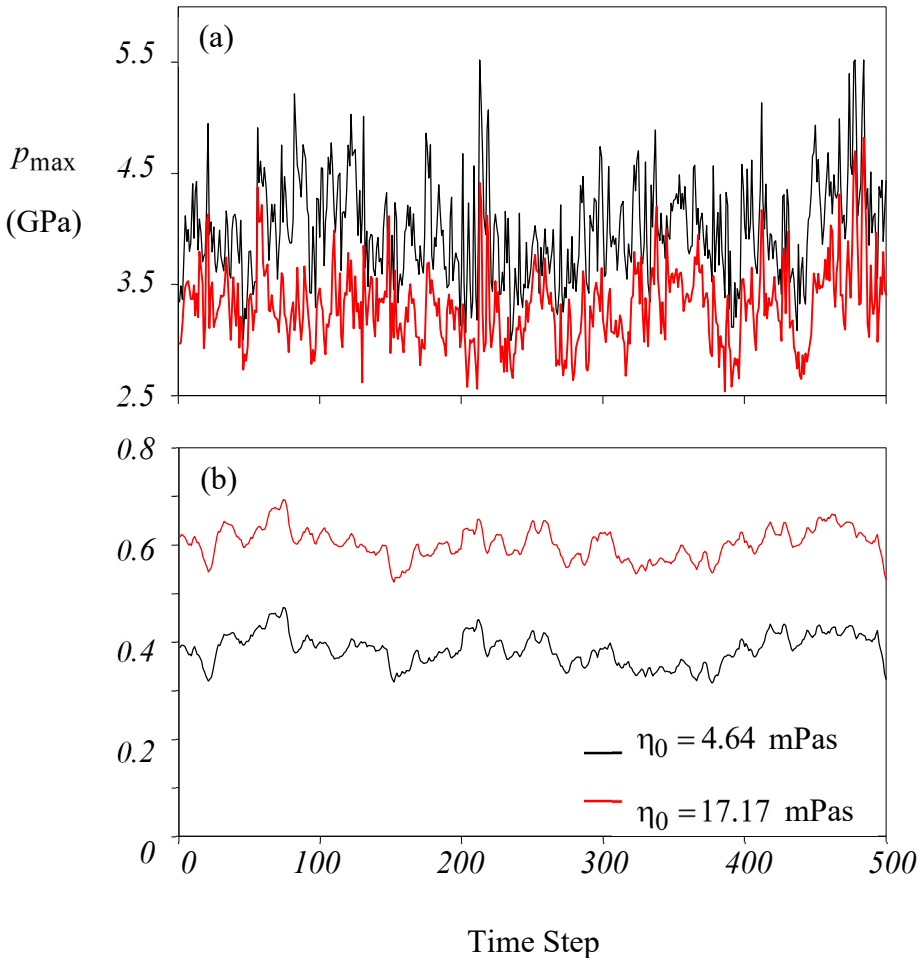

Figure.3.23 Variations of (a) maximum contact pressure, and (b) Hertzian zone Average film thickness with time for surface of R_q=0.3μm operating under P_h=1.75 GPa and h^{in} =10 μm.

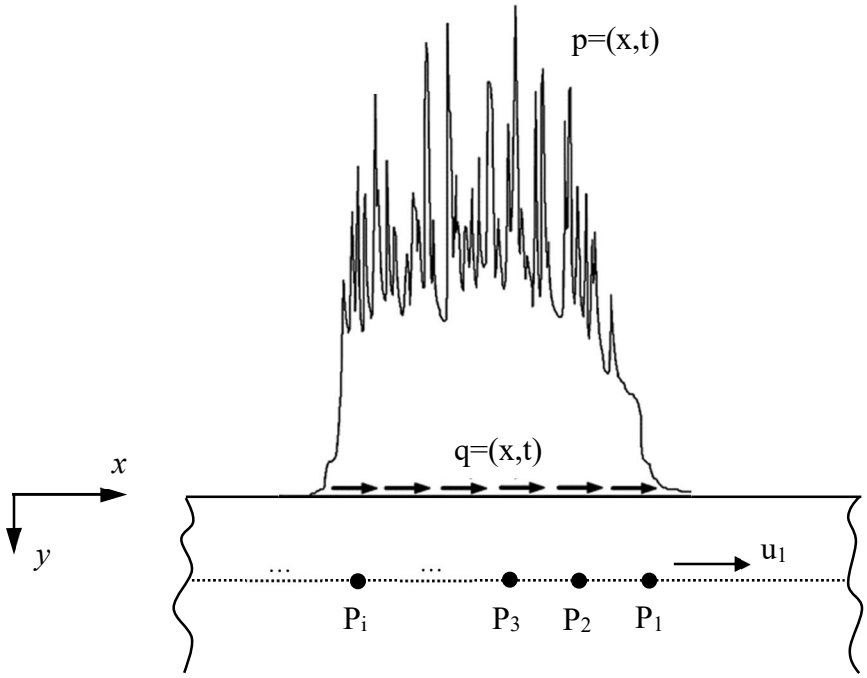

Figure.3.24 Schematic view of material points (P_i) passing through computational domain as contact body rolls.

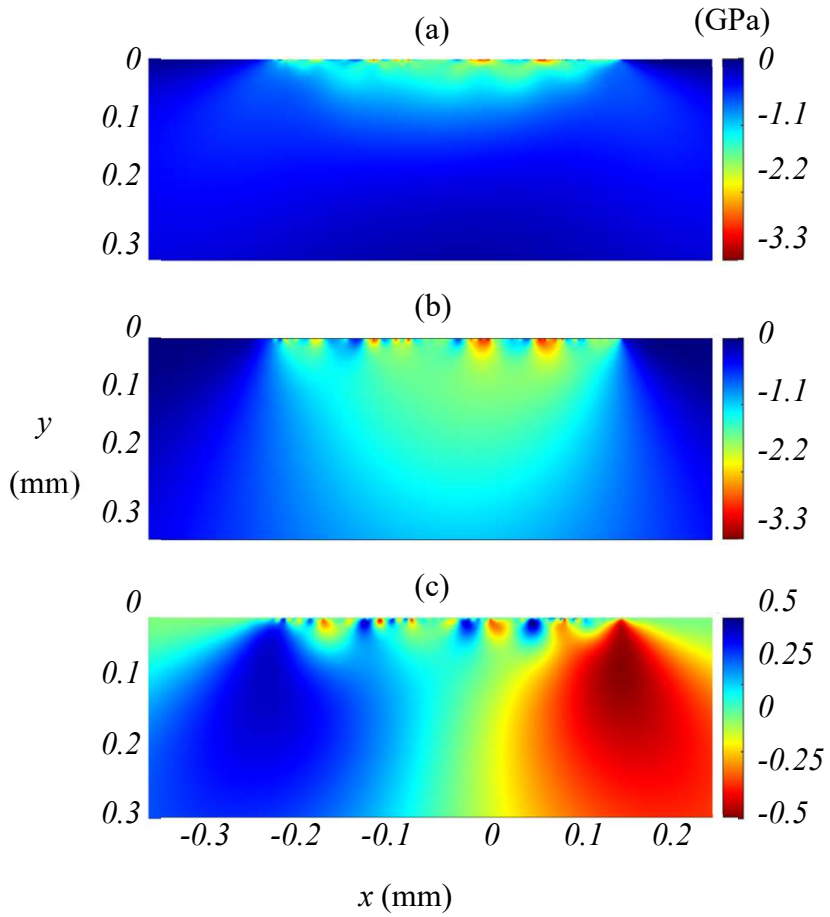

Figure.3.25 Distributions of (a) σ_x, (b) σ_y, and (c) σ_{xy}, under surface pressure and shear

Conditions defines in the left column of Figure.3.2.

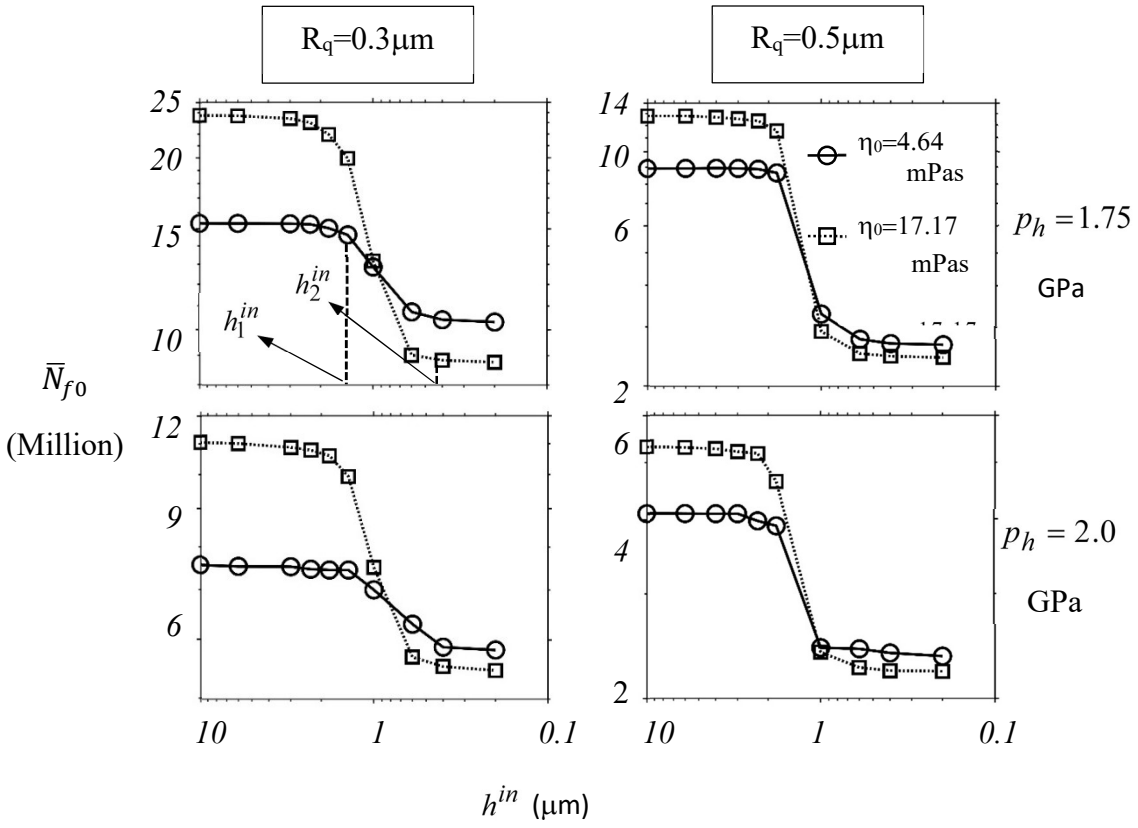

Figure.3.26 Variations of median fatigue life, $\bar{N}_{f0}$, with supplied inlet film thickness, h^{in}. Left and right columns represent simulations with low and high roughness amplitudes respectively. Top and bottom rows represent simulations with low and high pressures, respectively.

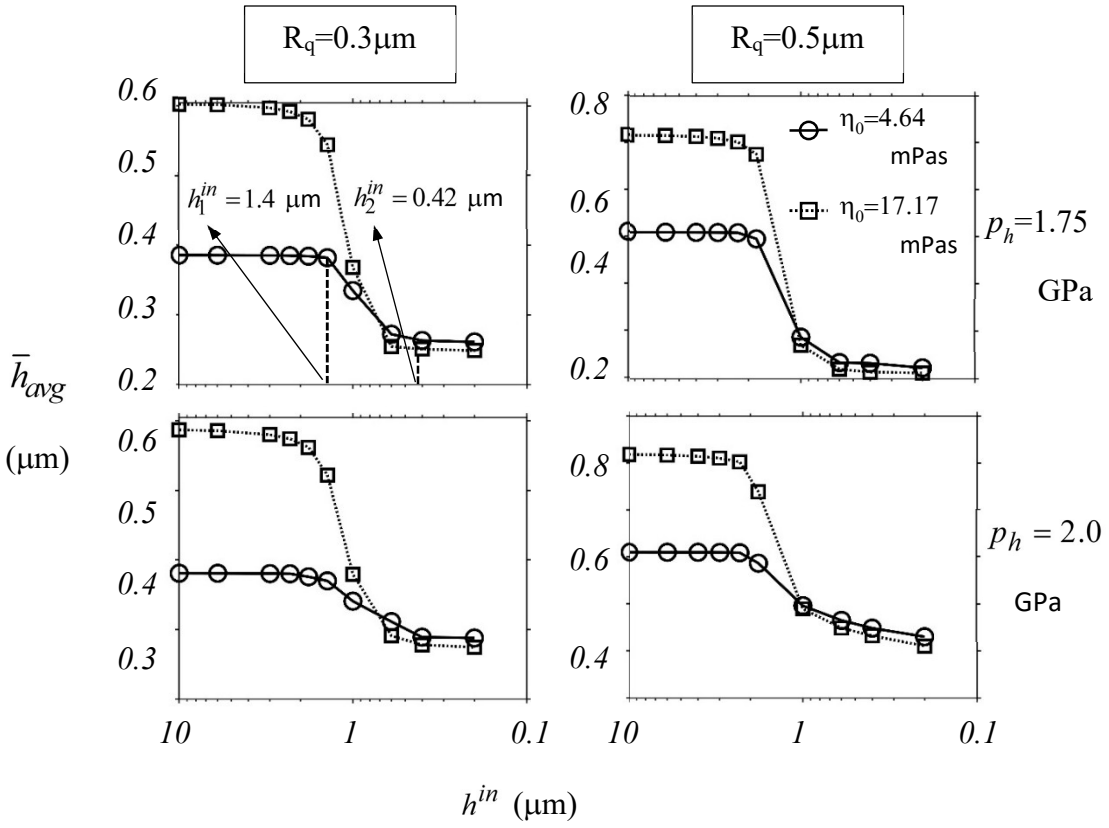

Figure.3.27 Variations of median Hertzian zone average film thickness, $\bar{h}_{avg}$, with Supplied inlet film thickness, h^{in} . Left and right columns represent simulations with low and high roughness amplitudes, respectively. Top and bottom rows represent simulations with low and high pressures, respectively.

Considering the baseline simulation, i.e. the first data point of the solid curve in the top left plot in Figure.3.27, the Hertzian zone average film thickness under this fully flooded lubrication condition is $\bar{h}_{avg}^{fld} = \bar{h}_{avg|h^{in}=1\ \mu m} = 0.386\mu m$. As h^{in} decreases from its baseline value of 10 μm while still being above the first threshold of $h_1^{in} = 1.4\mu m$, $\bar{h}_{avg}$ is barely affected, since the supplied film thickness, h^{in}, is much larger than $\bar{h}_{avg}^{\text{fld}}$ and thus no starvation is induced. When h^{in} drops below h_1^{in}, it becomes more comparable to the fully flooded average film thickness, under which circumstance, starvation was reported to start to impact the lubrication film thickness within the contact zone [26, 43]. As a result, rapid decrease in $\bar{h}_{avg}$ follows as shown in Figure.3.27. Regarding the second threshold, h_2^{in}, below which the curves return to their initial flatness, it was found to be closely related to the composite surface roughness RMS amplitude, R_q^c [29]. In this study, $R_q^c = 0.42$ μm and 0.71 μm for the two roughness profiles considered. In the left and right columns of Figure.3.27, h_2^{in} is observed to be in the vicinity of 0.42 μm and 0.71 μm, respectively. Below this second threshold that is defined by roughness, the two surfaces in contact do not allow further large rigid body approach to ensure the equilibrium of Eq. (2.27) is maintained [29]. Consequently, the Hertzian zone average film thickness decreases very slightly after h^{in} drops below. h_2^{in} Recognizing the inverse relationship between contact pressure and lubrication film thickness, as well as between surface shear and film thickness, the variation of $\bar{h}_{avg}$ with h^{in} in Figure.3.27 leads to the patterns of pressure dependence and friction dependence on h^{in}, as shown in Figures.3.28 and 3.29, respectively.

Both the median of maximum contact pressure, $\bar{p}_{max}$, and the median of friction coefficient, $\bar{\mu}$, are raised sharply only between the two thresholds of the supplied inlet lubrication film thickness, therefore, resulting in the fatigue life behavior in Figure.3.26.

Revisiting Figure.3.26, the solid curves are compared with the dotted ones to examine the lubricant viscosity effect on fatigue life. It is observed, very interestingly, the improvement in fatigue performance with higher lubricant viscosity diminishes as h^{in} decreases and escalates lubrication starvation. Surprisingly, after the lubrication is sufficiently starved, higher viscosity is seen to even reduce, instead of elongating, the fatigue life. For instance, under the surface condition of R_q=0.3μm and low load condition of p_h =1.75 GPa, the fatigue life is effectively increased from 15.34 million cycles to 23.71 million cycles (a 54.6 % rise) under fully flooded lubrication condition at h^{in} =10 μm, by implementing a higher viscosity. However, at $h^{in} = 0.2$μm, where the lubrication is severely starved, the life is reduced from 10.31 million cycles to 8.77 million cycles, leading to a 14.9 % decline, when η_0 is raised from 4.64 mPas to 17.17 mPas. The fatigue life changes under the other three roughness and load combinations are recorded and compared in Table 2.

To find the underlying physical cause of the reverse effect of lubricant viscosity on fatigue under lubrication starvation, Figures.3.27-3.29 are reviewed for the behavior of film thickness, pressure and friction when viscosity is varied. Adopting a higher viscosity, it is seen the film thickness is generally higher before severe starvation takes place. becomes lower afterwards. This lower film thickness leads to the higher pressure as shown in Figure.3.28, and contributes to the higher surface shear (more asperity interactions) as shown fig.3.29.

Table 2 Median fatigue life, $\bar{N}_{f0}$, summary for viscosity effect comparison.

$\bar{N}_{f0}$ (Million)			$R_q = 0.3$ μm			$R_q = 0.5$ μm		
			η_0 (mPas)		$\bar{N}_{f0}$ Improvement (%)	η_0 (mPas)		$\bar{N}_{f0}$ Improvement (%)
			4.64	17.17		4.64	17.17	
$p_h = 1.75$ (GPa)	h^{in} (μm)	10	15.34	23.71	54.6	8.92	12.80	43.5
		0.2	10.31	8.77	-14.9	2.66	2.44	-8.2
$p_h = 2.0$ (GPa)	h^{in} (μm)	10	7.56	11.05	46.2	4.10	5.31	29.5
		0.2	5.82	5.46	-6.2	2.36	2.22	-5.9

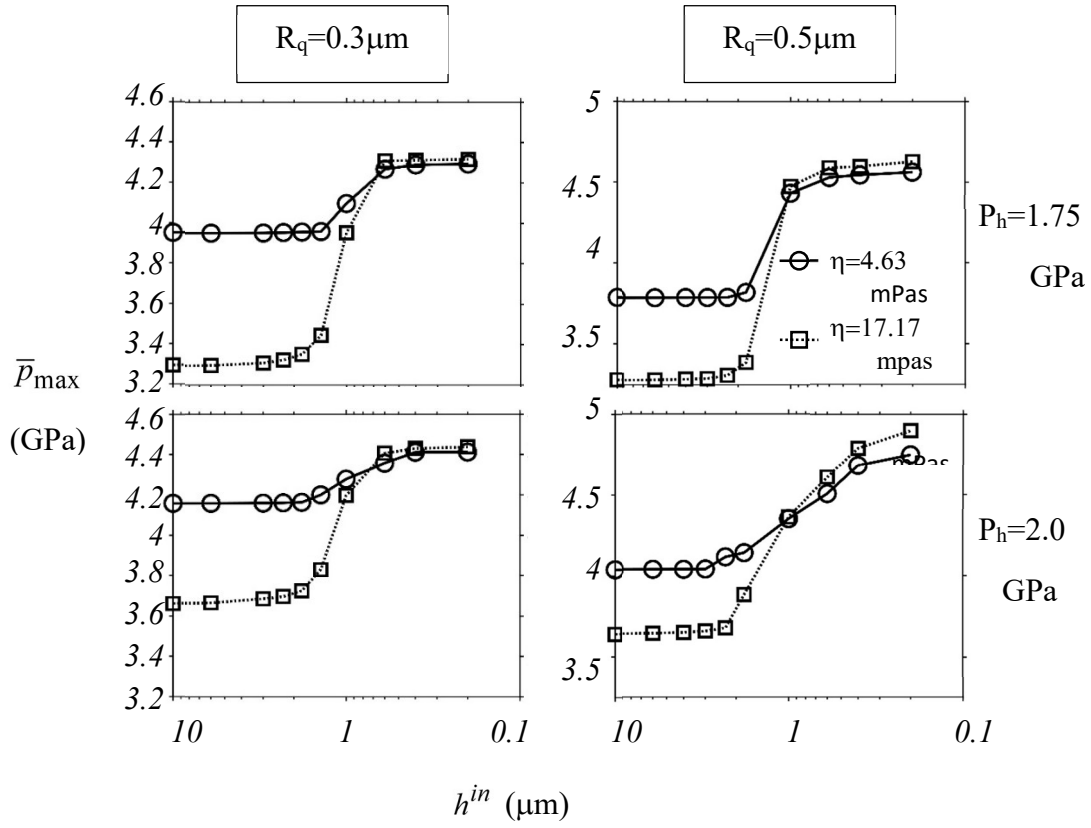

Figure.3.28 Variations of median maximum contact pressure, $\overline{p}_{max}$, with supplied inlet Film thickness, h^{in}. Left and right columns represent simulations with low and high roughness amplitudes, respectively. Top and bottom rows represent simulations with low and high pressures, respectively.

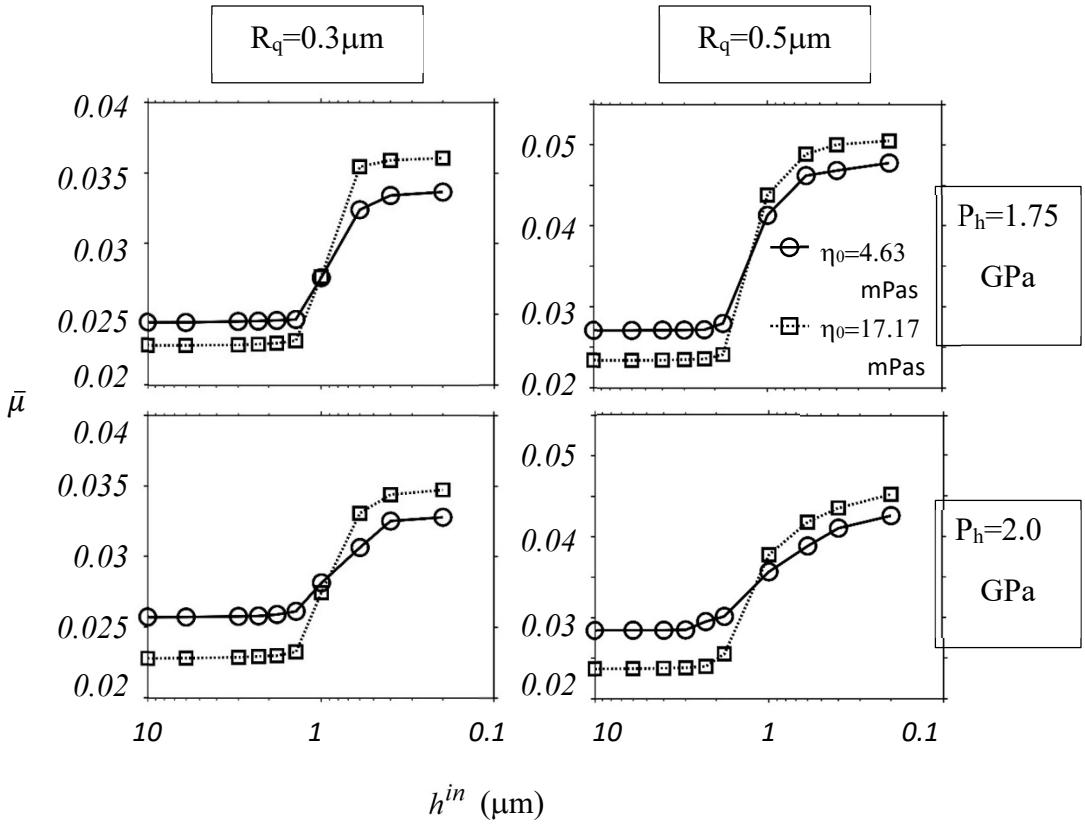

Figure.3.29 Variations of median friction coefficient, $\bar{\mu}$, with supplied inlet film thickness, h^{in}. Left and right columns represent simulations with low and high roughness amplitudes, respectively. Top and bottom rows represent simulations with low and high pressures, respectively.

Additionally, the higher viscosity directly affects the friction by increasing the viscous shear within the fluid areas. For a more detailed illustration, the transient tribological behavior under the two viscosity conditions are compared, in Figure.3.30, for the smoother rough surface operating under the low load and the most starved lubrication condition, i.e. $p_h = 1.75$ GPa and $h^{in} = 0.2$ μm. More asperity contacts are observed when η_0 is increased from 4.64 mPas to 17.17 mPas to introduce sharp increases in both pressure and surface shear peaks. The local cavitation at = -0.135 μm, in the right plot of Figure.3.30 (c), is responsible for the highest *p* and *q* peaks when $\eta_0 = 17.17$ mPas is implemented. The elevated *p* and *q* directly impact the multi-axial stress fields and thus leading to lower fatigue lives in Figure.3.26, under highly starved lubrication condition.

These reverse effects of lubricant viscosity on film thickness, pressure, shear, and fatigue life, under lubrication starvation, contradict the widely accepted EHL rules under fully flooded lubrication condition, which state higher viscosity leads to better lubrication performance in terms of film thickness and failure prevention [5]. In the light of the experimental measurements of film thickness by Cann [1], this contradiction seems to be valid. It was shown by the experiments that absolute film thickness was increased by moving from high viscosity base oil to a lower one when starvation was in effect [1]. It is postulated the supplied inlet lubrication film thickness, h^{in}, may not be a good measure of the extent of starvation. Instead, the ratio of the supplied film thickness to the fully flooded lubrication film thickness, $\chi_h = h^{in} / \bar{h}_{avg}^{\text{fld}}$, may be a better indicator.

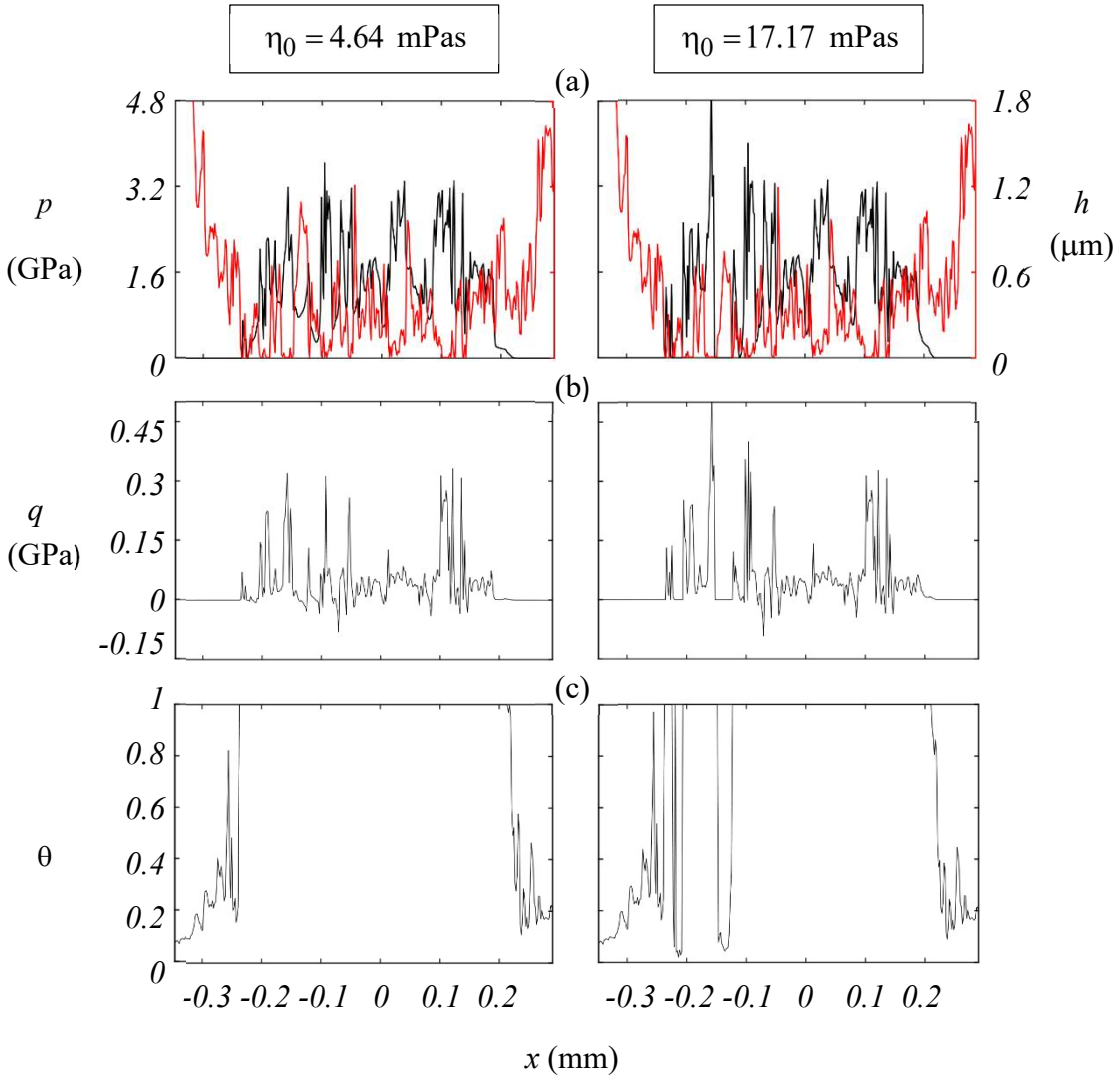

Figure.3.30 Transient distributions of (a) contact pressure (black) and lubrication film thickness (red), (b) surface shear, and (c) film fraction parameter for surface of R_q=0.3μm operating under $p_h = 1.75$ GPa and $h^{in} = 0.2$ μm.

For instance, considering the low load and roughness amplitude combination in Figure.3.26, the fully flooded lubrication condition leads to the Hertzian zone average film thickness $\bar{h}_{avg}^{\text{fld}} = 0.386$ μm and 0.603 μm for $\eta_0 = 4.64$ mPas and 17.17 mPas, respectively. It can be stated, alternatively, that $\bar{h}_{avg}^{\text{fld}} = 0.386$ μm and 0.603 μm is required for fully flooded lubrication under the low and high viscosity conditions, respectively. Thus, with the same supplied fluid film thickness of $h^{in} = 0.2\mu$m, χ_h yields 0.52 for the low viscosity case, which is much higher than $\chi_h = 0.33$ for the high viscosity condition. The higher χ_h ratio means more lubricant supply in reference to the required amount of lubricant for fully flooded lubrication, leading to thicker $\bar{h}_{avg}$ in Figure.3.27, lower $\bar{p}_{\max}$ in Figure.3.8, lower friction in Figure.3.29, and therefore higher fatigue life in Figure.3.26.

Another interesting behavior of the film thickness, recorded in Figure.3.27 (upper row versus lower row), is that, under fully flooded condition, the film thickness under lower load is slightly higher than that under higher load, which is as expected; however, under starved lubrication condition, the film thickness becomes smaller when the load is decreased. This reverse phenomenon can be explained in a similar way that explains the reverse film thickness behavior under low and high lubricant viscosities. The average film thickness under fully flooded condition for the low load case is higher than that for the high load case, indicating the former requires more lubrication fluid than the latter.

Thus, with the same amount of limited lubricant supply, the low load case experiences more severe starvation, resulting in lower average film thickness in the nominal Hertzian zone. Additionally, a higher load contributes to faster establishment of pressurized EHD fluid film in inlet zone when lubrication is starved.

As compared in Figure.3.31 (c) for the rougher surface operating under $\eta_0 = 4.64$ mPas and $h^{in} = 1.0\,\mu$m, for instance, the fluid film fraction parameter, climbs to the value of 1, i.e. pressurized EHD film is formed, at $X_{menicus}$= -0.22 μm for the low load case, and -0.32 μm for the high load scenario. Using the half Hertzian widths of the two loads of a_h =0.23 μm and 0.27μm, the normalized inlet meniscus location, $\bar{x}_{\text{menicus}} = x_{\text{menicus}}/a_h = -0.96$, and -1.18, respectively, for the low and high load conditions. This more effective EHD film formation under higher load is believed to be also responsible for the higher film thickness when lubrication is starved. It is noted, although with the higher film thickness, the larger pressure and shear as shown in Figure.3.31 (a) and (b) under higher load still leads to smaller fatigue lives as listed in Table 2 in comparing to the low load condition.

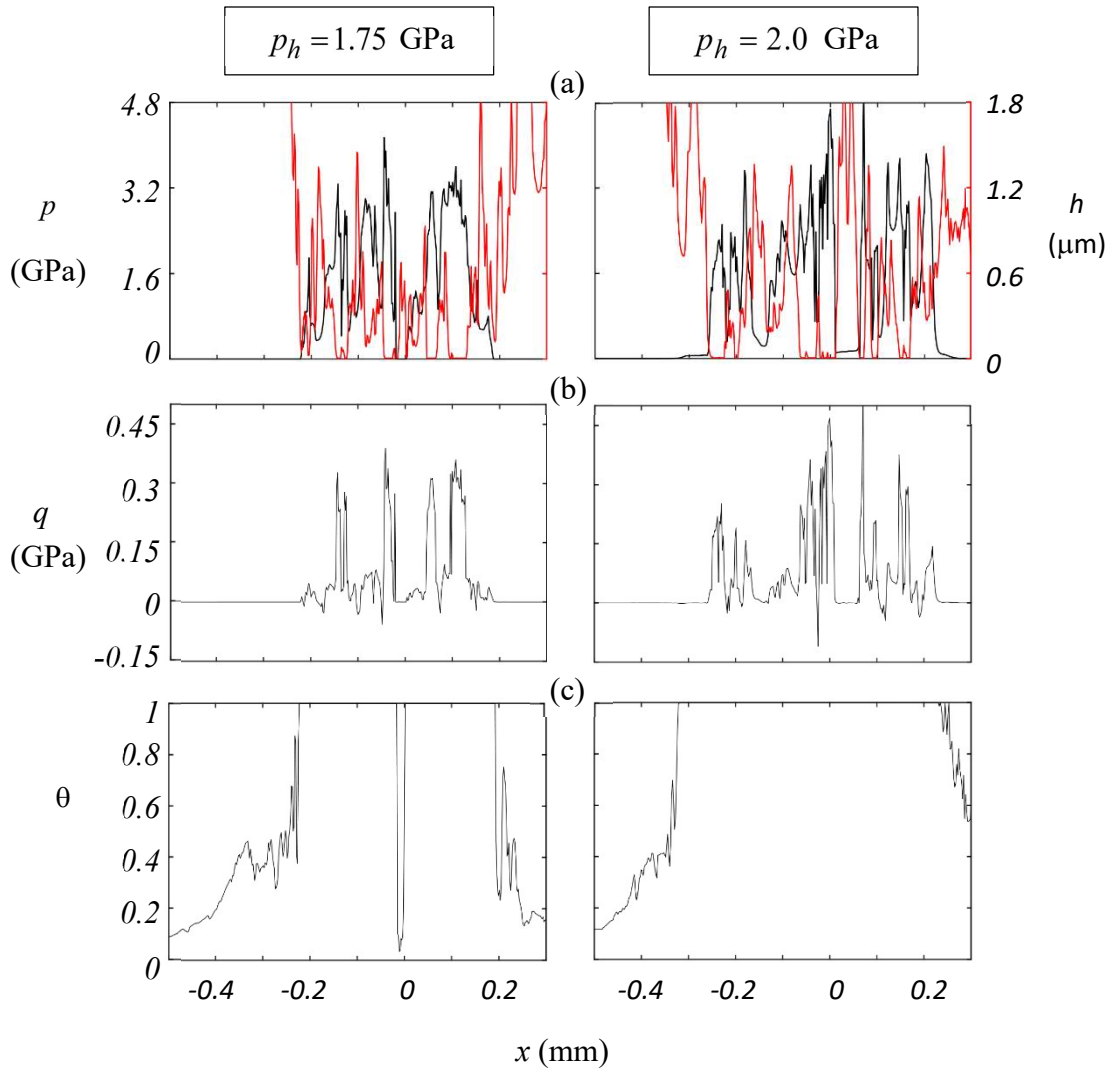

Figure.3.31 Transient distributions of (a) contact pressure (black) and lubrication film thickness (red), (b) surface shear, and (c) film fraction parameter for surface of $R_q = 0.5$ μm operating under $\eta_0 = 4.64$ mPas and $h^{in} = 1$ μm.

CHAPTER -4

CONCLUSION AND FUTURE WORKS

4.1 CONCLUSIONS

In this study, a contact fatigue model for line contacts operating under starved lubrication condition is proposed. Incorporated with a film fraction parameter, a mixed lubrication formulation that is applicable for both fully flooded and starved lubrication conditions is employed to determine the surface normal pressure and tangential shear. The stress fields produced by these surface tractions are evaluated assuming a half space contact problem, since the contact zone is small in comparing to the body itself. Implementing a fatigue criterion, the amplitudes and mean of the multi-axial stress components are used to assess the fatigue damage. Considering different surface roughness amplitudes, Hertzian contact pressures, and lubricant viscosities, parametric simulations are carried out within a range of supplied inlet lubricant film thickness, which is varied to introduce different starvation severity. The observations are summarized as follow

- Significant fatigue life reduction occurs only when the supplied inlet lubrication film thickness is sufficiently small, say comparable to the average film thickness within the nominal Hertzian zone under fully flooded lubrication condition.
- After the supplied inlet lubrication film thickness drops below the composite surface roughness RMS amplitude, further decreases in fatigue life become very limited.

- Regarding surface roughness and contact load effects on fatigue life, as expected, rougher surface and heavier load leads to lower fatigue life under both fully flooded and starved lubrication conditions.

Surprisingly and Interestingly, lower lubricant viscosity is shown to be able to elongate the fatigue life when lubrication is starved, which is opposite to the EHL rule under fully flooded lubrication condition, stating higher viscosity results in thicker lubrication film and improved fatigue life.

4.2. RECOMMENDATIONS FOR FUTURE WORKS

The numerical results presented here have offered a lot of information about the effects of lubrication starvation on gear contacts and their susceptibility to contact fatigue failure for realistic engineering surfaces under typical automotive speed operating conditions, with robust models used for all lubricant properties. Still, many aspects could be better understood with further numerical and experimental investigations.

A significant assumption is made in the contact fatigue model concerning the boundary lubrication friction coefficient. For the results presented here, a constant value of 0.1 was employed, which is reasonable for the boundary layer lubrication regime. However, it is well-known that the friction coefficient increases as the amount of lubrication decreases and so it is not certain whether the chosen constant friction coefficient is the most accurate for differing amounts of lubrication starvation. To increase the fidelity of the model, future work could focus on experimental characterization of different lubricants under a range of lubrication starvation severity and the results could then be incorporated into the computational model.

REFERENCE

[1] Cann, P. M., 1999, Starved grease lubrication of rolling contacts, Tribology Transaction, 42(4), 867–873.

[2] Fujita, K., and Yoshida, A., 1981, Effects of hardness difference on the surface durability and surface failure of steel rollers, Wear, 67, 187–200.

[3] Fujita, K., and Yoshida, A., 1984, Effects of molybdenum disulphide and an organic molybdenum compound in gear oil on rolling contact fatigue, Wear, 95, 271–286.

[4] Ioannides, E., and Harris, T. A., 1985, A new fatigue model for rolling bearings, ASME Journal of Tribology, 107(3), 367–377.

[5] Li, S., and Kahraman, A., 2011, A fatigue model for contacts under mixed elestrohydrodynamic lubrication condition, International Journal of Fatigue, 33, 427–436.

[6] Li, S., Kahraman, A., and M. Klein, 2012, A fatigue model for spur gear contacts operating under mixed elastohydrodynamic lubrication conditions, ASME Journal of Mechanical Design,134, 041007(11 pages).

[7] Hoffmann, G., Hanejko, F. G., and Slattery, R. H., 2006, Crack initiation and propagation in RCF - a new approach to understanding pitting failure of highly loaded gears. SAE World Congress, Detroit, USA.

[8] Li, S., Kahraman, A., 2013, Micro-pitting fatigue lives of lubricated point contacts: Experiments and model validation, International Journal of Fatigue, 48, 9–18.

[9] Li, S., and Kahraman, A., 2009, A mixed EHL model with asymmetric integrated control volume discretization, Tribology International, 42(8), 1163–1172.

[10] Li, S., and Kahraman, A., 2010, A transient mixed elastohydrodynamic lubrication model for spur gear pairs, ASME Journal of Tribology,132, 011501 (9 pages).

[11] Cusano, C., and Wedeven, L. D., 1982, The effects of artificially-produced defects on the film thickness distribution in sliding EHD point contacts, Journal of Lubrication Technology, 104, 365–375.

[12] Li, S., and Parmar, U., 2018, The effects of micro dimple texture on the friction and thermal behavior of a point contact, ASME Journal of Tribology, 140, 041503.

[13] Snidle, R. W., and Evans, H. P., 2010, Mixed lubrication and prediction of surface fatigue in gear tooth contacts, Proceedings of International Conference on Gears, Technical University of Munich, October 2010, VDI-Berichte, Dusseldorf, Germany, VDI-Berichte No. 2108.

[14] Zhu, D., Ren, N., and Wang, Q. J., 2009, Pitting life prediction based on a 3D line contact mixed EHL analysis and subsurface von Mises stress calculation, Journal of Tribology, 131(4), 041501 (6 pages).

[15] Epstein, D., Keer, L. M., Wang, Q. J., Cheng, H. S., and Zhu, D., 2003, Effect of surface topography on contact fatigue in mixed lubrication, Tribology Transaction, 46(4), 506–513.

[16] Li, S., and Anisetti, A., 2017, A tribo-dynamic contact fatigue model for spur gear pairs, International Journal of Fatigue, 98, 81–91.

[17] Meheux, M., Minfray, C., Ville, F., Mogne, T. L., Lubrecht, A. A., Martin, J. M., Lieurade, H. P., and Thoquenne, G., 2010, Effect of lubricant additives in rolling contact fatigue, Proceedings of the Institution of Mechanical Engineers, Part J: Journal of Engineering Tribology, 224(9), 947–955.

[18] Yoshioka, T., Shimizu, S., and Shimoda, H., 2009, A new rolling contact damage of deep groove ball bearing under grease lubrication, Tribology Transaction, 42(4), 867–873.

[19] Riggs, M. R., Murthy, N. K., and Berkebile, S. P., 2017, Scuffing resistance and starved lubrication behavior in helicopter gear contacts: dependence on material, surface finish, and novel lubricants, Tribology Transactions, 60(5), 932–941.

[20] Enthoven, J., and Spikes, H. A., 1996, Infrared and visual study of the mechanisms of scuffing, Tribology Transactions, 39(2), 441–447.

[21] Ali, F., Krupka, I., and Hartl, M., 2013, Analytical and experimental investigation on friction of non-conformal point contacts under starved lubrication, Meccanica, 48(3), 545–553.

[22] Lewis, S. R., Lewis, R., Evans, G., and Buckley-Johnstone, L. E., 2014, Assessment of railway curve lubricant performance using a twin-disc tester, Wear, 314, 205–212.

[23] Querlioz, E., Ville, F., Lenon, H., and Lubrecht, T., 2007, Experimental investigations on the contact fatigue life under starved conditions, Tribology International, 40, 1619–1626.

[24] Labiau, A., Ville, F., Sainsot, P., Querlioz, E., Lubrecht, T., 2008, Effect of sinusoidal surface roughness under starved conditions on rolling contact fatigue, Proceedings of the Institution of Mechanical Engineers, Part J: Journal of Engineering Tribology, 222, 193–200.

[25] Hamrock, B. J., and Dowson, D., 1977, Isothermal elastohydrodynamic lubrication of point contacts, part IV, Starvation results, Journal of Lubrication Tech, 99(1), 15–23.

[26] Chevalier, F., Lubrecht, A. A., Cann, P. M. E., Colin, F., and Dalmaz, G., 1998, Film thickness in starved EHL point contacts, ASME Journal of Tribology, 120(1), 126–133.

[27] Yang, P., Wang, J., and Kaneta, M., 2006, Thermal and non-Newtonian numerical analyses for starved EHL line contacts, ASME Journal of Tribology, 128(2), 282–290.

[28] Pu, W., Zhu, D., and Wang, J., 2018, A starved mixed elastohydrodynamic lubrication model for the prediction of lubrication performance, friction and flash temperature with arbitrary entrainment angle, ASME Journal of Tribology, 140(3), 031501 (12 pages).

[29] Li, S., and Masse, D., 2019, On the flash temperature under starved lubrication condition of a line contact, Tribology International, 136, 173–181.

[30] Elrod, H. G., 1981, A cavitation algorithm, ASME Journal of Lubrication Technology, 103(3), 350–354.

[31] Li, S., and Anisetti, A., 2016, On the flash temperature of gear contact under the tribo-dynamic condition, Tribology International, 97, 6–13.

[32] Li, S., Kahraman, A., Anderson N. E., and Wedeven, L. D., 2013, A model to predict scuffing failures of a ball-on-disk contact, Tribology International, 60, 233–245.

[33] Bair, S., and Winer, W. O., 1993, A new high-pressure, high-shear stress viscometer and results for lubricants, Tribology Transactions, 36(4), 721–725.

[34] Schmidt, K., Bair, S., and Trusler, J. P. M., The viscosity of squalane revisited – an updated reference model, 16th Meeting of the International Association for Transport Properties, July 15th, 2016, Imperial College London, U.K.

[35] Bair, S., 2007, High-pressure Rheology for quantitative elastohydrodynamics, Elsevier Science, Amsterdam.

[36] Johnson, K. L., Contact Mechanics, Cambridge University Press, Cambridge, 1985.

[37] Li, S., 2014, A boundary element model for near surface contact stresses of rough surfaces, Computational Mechanics, 54(3), 833–846.

[38] Matake, T., 1977, An explanation of fatigue limit under combined stress, Bull. JSME, 20, 257–263.

[39] McDiarmid, D. L., 1994, A shear stress based critical-plane criterion of multiaxial fatigue failure for design and life prediction, Fatigue & Fracture of Engineering Materials & Structures, 17, 1475–1484.

[40] Susmel, L., and Lazzarin, P., 2003, A stress-based method to predict lifetime under multiaxial fatigue loadings, Fatigue & Fracture of Engineering Materials & Structures, 26, 1171–1187.

[41] Liu, Y., and Mahadevan, S., 2007, A unified multiaxial fatigue damage model for isotropic and anisotropic materials, International Journal of Fatigue, 29, 347–359.

[42] Zaretsky, E. V., 1987, Fatigue criterion to system design, life and reliability, Journal of Propulsion and Power, 3, 76–83.

[43] Svoboda, P., Kostal, D., Krupka, I., and Hartl, M., 2013, Experimental study of starved EHL contacts based on thickness of oil layer in the contact inlet, Tribology International, 67, 140–145.

[44] A.R. Hassan. Contact Stress Analysis of Spur Gear Teeth Pair. World Academy of Science, Engineering and Technology, 58: 611-616, 2009.